Intraparticle Kinetics Unveil Crowding and Enzyme Distribution Effects on the Performance of Cofactor-Dependent Heterogeneous Biocatalysts

Eleftheria Diamanti, Javier Santiago-Arcos, Daniel Grajales-Hernández, Nicolette Czarnievicz, Natalia Comino, Irantzu Llarena, Desiré Di Silvio, Aitziber L. Cortajarena, and Fernando López-Gallego*

ABSTRACT: Multidimensional kinetic analysis of immobilized enzymes is essential to understand the enzyme functionality at the interface with solid materials. However, spatiotemporal kinetic characterization of heterogeneous biocatalysts on a microscopic level and under *operando* conditions has been rarely approached. As a case study, we selected self-sufficient heterogeneous biocatalysts where His-tagged cofactor-dependent enzymes (dehydrogenases, transaminases, and oxidases) are co-immobilized with their corresponding phosphorylated cofactors [nicotinamide adenine dinucleotide phosphate (NAD(P)H), pyridoxal phosphate (PLP), and flavin adenine dinucleotide (FAD)] on porous agarose microbeads coated with cationic polymers. These self-sufficient systems do not require the addition of exogenous cofactors to function, thus avoiding the extensive use of expensive cofactors. To comprehend the microscopic kinetics and thermodynamics of self-sufficient systems, we performed fluorescence recovery after photobleaching measurements, time-lapse fluorescence microscopy, and image analytics at both single-particle and intraparticle levels. These studies reveal a thermodynamic equilibrium that rules out the reversible interactions between the adsorbed phosphorylated cofactors and the polycations within the pores of the carriers, enabling the confined cofactors to access the active sites of the immobilized enzymes. Furthermore, this work unveils the relationship between the apparent Michaelis−Menten kinetic parameters and the enzyme density in the confined space, eliciting a negative effect of molecular crowding on the performance of some enzymes. Finally, we demonstrate that the intraparticle apparent enzyme kinetics are significantly affected by the enzyme spatial organization. Hence, multiscale characterization of immobilized enzymes serves as an instrumental tool to better understand the *in operando* functionality of enzymes within confined spaces.
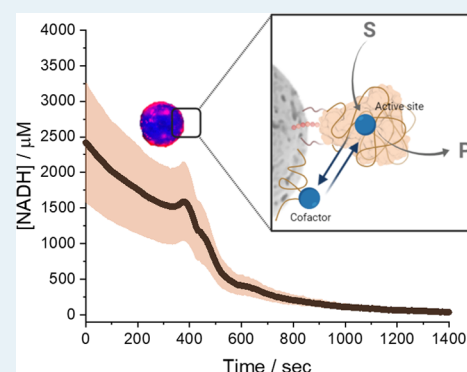
KEYWORDS: *protein immobilization, confined kinetics, heterogeneous biocatalysis, oxidoreductases, transaminases*

■ INTRODUCTION

Heterogeneous biocatalysis is a highly relevant matter in biotechnology, as immobilized enzymes are extensively applied in biotransformations at both industrial and academic levels.[1,2] Unlike homogeneous biocatalysis, where enzymes are soluble, heterogeneous biocatalysis involves enzymes either attached to or entrapped into solid materials. Well-designed protocols for enzyme immobilization on solid carriers improve several enzyme properties such as operational handling and stability that enhance the bioprocess efficiency.[3−6] Despite the great advances that immobilization technology has meant for applied biocatalysis, heterogeneous biocatalysts still face some intrinsic limitations (i.e., mass transfer restrictions, reactants, condition gradients, etc.) that need to be assessed to maximize the enzyme performance in the solid phase. To this aim, a multidimensional study of immobilized enzymes is essential to understand enzyme functionality at the interface with solid materials. Unlike chemical heterogeneous catalysts,[7] spatio-

temporal functional characterization of immobilized enzymes has been rarely approached at the microscopic level and under *operando* conditions.

Kinetics of the immobilized enzymes are fundamental to understand their operational performance and guide their optimization when their industrial application is aimed. The catalytic efficiency of immobilized enzymes is usually measured in liquid bulk solutions and compared with their corresponding soluble counterparts that are measured under substrate saturating conditions and at low enzyme concentrations. However, immobilized enzymes work under confined and
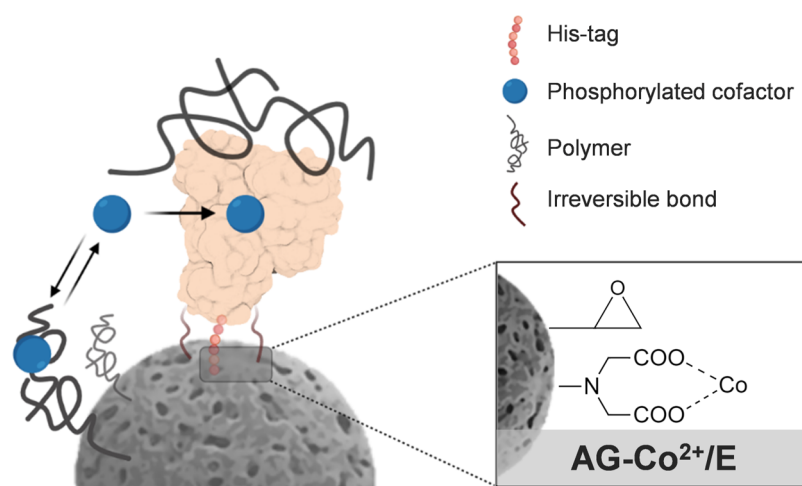
Figure 1. Schematic illustration of porous agarose microbeads functionalized with cobalt chelates and epoxy groups for the site-selective irreversible enzyme immobilization and the assembly of the cationic polymers for the subsequent cofactor co-immobilization.

crowded microenvironments where substrate diffusion issues, excluded volume effects, nonspecific binding of reactants, and reaction condition gradients greatly affect enzyme functionality.[8,9] Despite providing valuable macroscopic information about the average performance of immobilized enzymes under real operational conditions, conventional *in vitro* activity assays underrepresent the abovementioned effects and miss the particle-to-particle functional variability underlying heterogeneous biocatalysts. For instance, bulk studies fail to identify inter and intraparticle variations in density, distribution, and activity of immobilized enzymes. Hence, most of the bulk studies usually conclude that enzymes alter their functionality upon the immobilization process, but the physicochemical reasons behind these alterations are rarely identified. Similar issues occurred in cell biology until *in vivo* single-cell studies prompted to shed light on the performance of enzymes within the cells.[10−12] Inspired by single-cell approaches based on fluorescence microscopy and/or spectroscopy, the structure, function, and spatial organization of enzymes supported on solid materials have been studied with spatiotemporal resolution, even reaching the single-molecule level.[13−18] However, most of these studies are carried out with system architectures (thin films, lipid layers, glass surfaces, etc.) that are hardly exploitable as heterogeneous biocatalysts for biomanufacturing/biosensing purposes. Hence, the quantitative assessment of complex intraparticle enzyme kinetics, protein localization, and mass transport issues remain elusive for ready-to-use enzymes supported on industrially relevant carriers (i.e., porous micro/nanoparticles, porous membranes, monoliths, electrodes, etc.).[19]
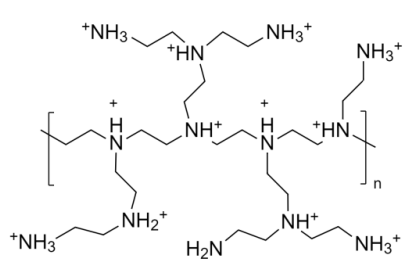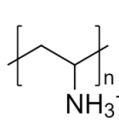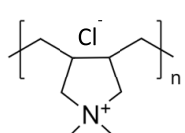
Even more challenging is the characterization of self-sufficient heterogeneous biocatalysts where a cofactor-dependent enzyme is co-immobilized with its corresponding cofactor on porous microparticles.[20] To this direction, carrier surfaces have been functionalized with positively charged amine groups that can electrostatically bind the phosphorylated cofactors, giving rise to a self-sufficient heterogeneous biocatalyst that does not require exogenous cofactor addition.[21,22] In this microscopic architecture, enzymes and cofactors are irreversibly attached and reversibly adsorbed to the carrier surface, respectively. Based on averaged macroscopic binding thermodynamics measured through bulk studies, cofactors are supposed to establish an association dissociation equilibrium

allowing them to shuttle between the active center of the enzymes without abandoning the carrier surface. Unfortunately, spatiotemporal information regarding the interplay between cofactors and enzymes within porous particles is scarce. This information is fundamental to characterize these advanced immobilized systems. Hence, single-particle measurements under *operando* conditions emerge as a fascinating approach to understand the microscopic dynamics of these self-sufficient heterogeneous biocatalysts.[13,14] Harnessing that many of the industrially relevant cofactors are phosphorylated and display fluorescence properties, our group has developed a time-lapse fluorescence microscopy method coupled with a routine for image processing and analysis to assess the activity of enzymes confined within porous materials.[23] However, this methodology misses multiplex information about the cofactor diffusion (thermodynamics), the enzyme and cofactor local concentrations, and their localization within a single particle.

In this work, we advance in characterizing the spatiotemporal performance of heterogeneous biocatalysts to better understand how kinetic parameters are linked to the density and the spatial organization of the enzyme across the solid surface of porous materials. We processed the images derived from time-lapse fluorescence microscopy experiments to determine intraparticle kinetics of self-sufficient heterogeneous biocatalysts made of His-tagged enzymes co-immobilized with their corresponding phosphorylated cofactors on porous agarose microbeads (Figure 1). Such microbeads were functionalized with both cobalt chelates and epoxy groups for enzyme immobilization and subsequently coated with cationic polymers.[24] Heterofunctional carriers are widely exploited for the site-directed immobilization and multivalent attachment of many enzymes used in applied biocatalysis.[24−26] As model enzymes, we herein selected four classes of industrially relevant enzymes: NADH-dependent alcohol dehydrogenase from *Bacillus stearothermophilus* (Bs-ADH),[27] flavin-dependent NADH oxidase from *Lactobacillus pentosus* (Lp-NOX),[28] NADPH-dependent ketoreductase from *Bacillus subtilis* (Bs-KRED),[29] and pyridoxal-dependent transaminase from *Pseudomonas fluorescence* (Pf-TA).[30] The resulting self-sufficient heterogeneous biocatalysts were then analyzed under both static and *operando* conditions to investigate the cofactor binding thermodynamics, the enzyme density, and the enzyme apparent Michaelis−Menten (MM) kinetics at both single-

Table 1. Binding Steady-State Thermodynamics of Different Phosphorylated Cofactors Adsorbed on AG-Co^{2+}/E Carriers Coated with Different Cationic Polymers (Protonated Chemical Structure Provided for Each Polymer)^{a}

	PEI			PAH			PDADMAC		
	Primary, Secondary, Tertiary			Primary			Quaternary		
cofactor	% Ψ^{b}	K_D (mM)	q_{max} (μmol g^{-1})	% Ψ	K_D (mM)	q_{max} (μmol g^{-1})	% Ψ	K_D (mM)	q_{max} (μmol g^{-1})
NADH	91	0.2 ± 0.02	8.1 ± 0.2	86	2.4 ± 0.6	49 ± 7.6	86	0.4 ± 0.04	26 ± 1.1
FAD	87	0.1 ± 0.03	14 ± 0.8	84	0.6 ± 0.1	8.6 ± 0.6	84	>500	>500
PLP	89	1.1 ± 0.24	67 ± 9.5	82	0.7 ± 0.1	38 ± 2.2	87	2.2 ± 0.9	52 ± 14
NADPH	92	0.3 ± 0.03	19 ± 0.5	93	0.5 ± 0.1	19 ± 1.2	ND^{c}	ND^{c}	ND^{c}

^{a}Equilibrium constant (K_D) and maximum adsorption capacity (q_{max}) were derived from Langmuir adsorption isotherms of NADH, flavin adenine dinucleotide (FAD), pyridoxal phosphate (PLP), and NADPH toward each polymer (bulk experiments). ^{b}Immobilization yield (% Ψ) was obtained as described in the Materials and Methods section. ^{c}Not determined.
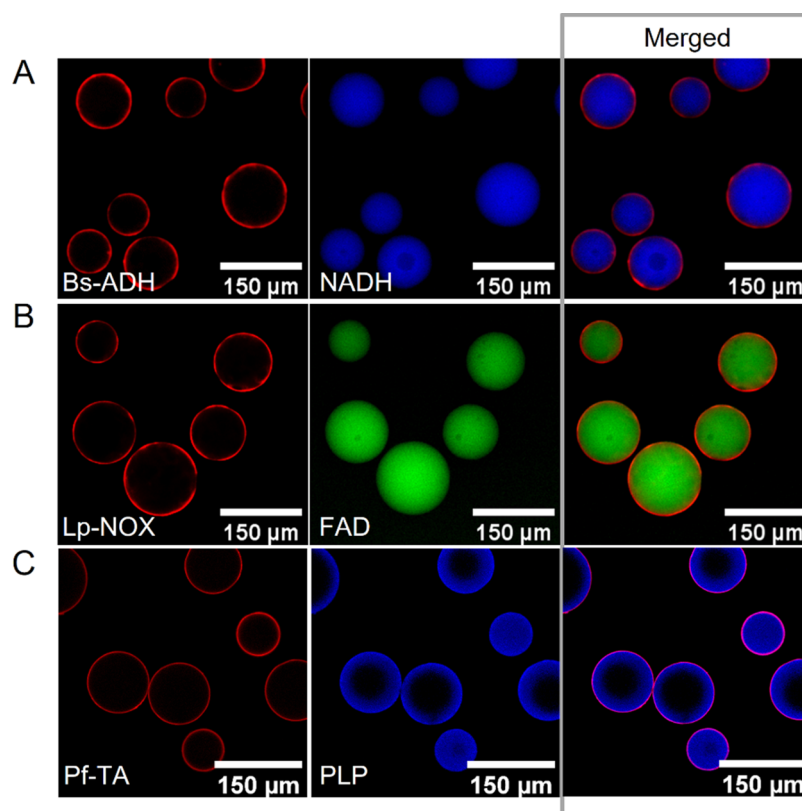

Figure 2. Spatial organization of enzymes and phosphorylated cofactors inside porous microbeads. Fluorescence microscopy images of (A) rhodamine B (RhB)-labeled Bs-ADH (red channel, λ_{ex}: 561 nm) co-immobilized with fluorescent NADH (blue channel, λ_{ex}: 405 nm), (B) RhB-labeled Lp-NOX (red channel, λ_{ex}: 561 nm) co-immobilized with fluorescent FAD (green channel, λ_{ex}: 488 nm) and (C) RhB-labeled Pf-TA (red channel, λ_{ex}: 561 nm) co-immobilized with fluorescent PLP (blue channel, λ_{ex}: 405 nm), on AG-Co^{2+}/E-PAH carriers.

particle and intraparticle levels. Our studies revealed that the enzyme concentration and spatial organization are the major sources of functional variability in these self-sufficient systems and have a significant impact on their intraparticle enzyme kinetics.

RESULTS AND DISCUSSION

Co-Immobilization of Enzymes and Cofactors. Initially, we immobilized His-tagged enzymes on porous agarose microbeads activated with cobalt chelates and epoxy groups (AG-Co^{2+}/E) as described in the Materials and Methods

section. As a result, the enzymes are oriented through their His-tag at the N-terminus and irreversibly attached to the surface of the carriers via covalent bonds formed between the epoxy groups and the Lys residues neighboring the His-tag (Figure 1).[31] Irreversible attachment of the enzymes to the AG-Co^{2+}/E surface was demonstrated by sodium dodecyl sulfate-polyacrylamide gel electrophoresis (SDS-PAGE) analysis (Figure S1). For the co-immobilization of the phosphorylated cofactors, the microbeads that harbor the immobilized enzymes were coated with the following cationic polymers (Figure 1): polyethyleneimine (PEI), polyallylamine (PAH), and polydiallyldimethylammonium chloride (PDADMAC), which contain different types of amines whose chemical structures are illustrated in Table 1. Upon enzyme immobilization, the remaining epoxy groups are the main attachment points for PEI and PAH, while PDADMAC is adsorbed to a negatively charged monolayer formed by previously blocking the remaining epoxy groups with aspartic acid. Prior to the cofactor adsorption, AG-Co^{2+}/E surfaces coated with the different polycationic polymers, AG-Co^{2+}/E-PEI, AG-Co^{2+}/E-PAH, and AG-Co^{2+}/E-PDADMAC, were characterized through X-ray photoelectron spectroscopy (XPS) (Figure S2 and Table S1). As expected, AG-Co^{2+}/E-PEI was formed by a combination of primary, secondary, and tertiary amine groups, AG-Co^{2+}/E-PAH mainly contained primary amines, and AG-Co^{2+}/E-PDADMAC majorly presented quaternary and secondary amines.

Previous studies showed that the phosphorylated cofactors are reversibly bound to surfaces coated with PEI; however, their binding to other positively charged polymeric coatings with different physicochemical properties is still unexplored. To study how phosphorylated cofactors bind to chemically diverse positive surfaces, we incubated nicotinamide adenine dinucleotide phosphate (NAD(P)H), FAD, and PLP in suspensions with AG-Co^{2+}/E-PEI, AG-Co^{2+}/E-PAH, and AG-Co^{2+}/E-PDADMAC under low ionic strength conditions. Table 1 shows that all cofactors were bound to all carriers with adsorption yields higher than 85%.

Next, we used AG-Co^{2+}/E-PAH as a model system to prove that NADH, FAD, and PLP can co-immobilize with their corresponding fluorescently labeled enzymes: Bs-ADH, Lp-NOX, and Pf-TA, respectively. Confocal laser scanning microscopy (CLSM) images showed that the enzymes did not colocalize with their corresponding cofactors across the porous surface at the microscopic level (Figure 2). While the enzymes are located at the outer surface of the porous microbeads, all cofactors but PLP are uniformly distributed across them.

According to the colocalization plots (Figure S3A,B), 5 and 4% of NADH and FAD populations were colocalized with Bs-ADH and Lp-NOX, respectively. In contrast, 18% of the PLP population was colocalized with the Pf-TA (Figure S3C) as PLP was less infiltrated into the surface of the porous microbeads. As previously reported by our group, PLP is bound to polymers containing positively charged primary amines through a dual interaction mode that involves the phosphate and aldehyde groups of PLP, which electrostatically and covalently react with the primary amines of the polymer coating, respectively.[32] Such dual interaction is not possible in NAD(P)H and FAD cofactors as they lack the aldehyde group. Therefore, the spatial distribution of the cofactors across the surface of the bead varies according to the chemical interactions they establish with the polymeric coatings.

Binding Thermodynamics of Phosphorylated Cofactors Adsorbed on Polymeric Coatings. Differences in adsorption yields and cofactor colocalization across the porous microbeads encouraged us to study the binding thermodynamics for each cofactor/cationic polymer pair under steady-state batch conditions (Table 1 and Figure S4). Langmuir adsorption isotherms showed that different polycationic coatings adsorbed each cofactor differently, depending on the type of amine groups, forming the polymeric coating. From the obtained Langmuir isotherms, we calculated the dissociation constants (K_D) that govern the reversible binding equilibria between the cofactors and the polycations. K_D values varied depending on the cofactor/cationic polymer pair (Table 1). While PEI and PDADMAC coatings adsorb NADH with similar K_D values, its adsorption on PAH coatings was less favorable. In contrast, PEI coatings bind FAD and NADPH with slightly lower K_D than those microbeads coated with PAH. Adsorption of FAD on PDADMAC did not follow a typical Langmuir isotherm, as the saturation plateau was not reached at the maximum offered concentration (4 mM), suggesting high K_D values for this cofactor/polymer pair.[33] XPS measurements (Table S1) showed that the surface of the microbeads is coated with different total densities of amine groups, depending on the polycation. Therefore, the cofactor adsorption phenomenon described herein relies on both the net charge of the polymer coating and the polymer density on the carrier surface as observed for other biomolecules.[34−37]

To demonstrate the intraparticle diffusion of the adsorbed cofactors, we performed fluorescence recovery after photobleaching (FRAP) measurements. For these studies, we selected the fluorescent FAD as a model cofactor to monitor its recovery inside the AG-Co^{2+}/E microbeads coated with PEI, PAH, or PDADMAC (Figure 3A). The average time of recovery after photobleaching of FAD on PEI-, PAH-, and PDADMAC-coated microbeads was less than 10 s in all cases (Figure 3B). Therefore, fast fluorescence recovery curves indicate that FAD rapidly reached a local equilibrium at any location within the bleach spot, pointing out an effective diffusion of the cofactor where binding dynamics are taking place.[38,39] Effective diffusion assumes that the binding reaction process is much faster than diffusion; therefore, FAD molecules may coexist as bound (on) and unbound (off) states within the carrier pores. In this context, model selection for fitting FRAP curves, where binding interactions are present, is a critical step.[38,40−42] Herein, we used the full reaction−diffusion model described elsewhere,[38] which includes all possible behaviors of recovery for a single binding reaction in the presence of diffusion. Therefore, the obtained FRAP curves were fitted (Figure 3B) with such a full reaction−diffusion model represented in the Laplace space (eq 1) according to Sprague et al.[38]

$$\overline{frap}(p) = \frac{1}{p} - \frac{F_{eq}}{p}\left(1 - 2K_1(qw)I_1(qw)\right) * \left(1 + \frac{k_{on}}{p + k_{off}}\right)$$
$$- \frac{C_{eq}}{p + k_{off}} \tag{1}$$

$$F_{eq} = \frac{k_{off}}{k_{on} + k_{off}} \tag{2}$$

$$C_{eq} = \frac{k_{on}}{k_{on} + k_{off}} \tag{3}$$

$$q^2 = \left(\frac{p}{D_f}\right)\left(1 + \frac{k_{on}}{p + k_{off}}\right) \tag{4}$$

where $\overline{frap}$ is the mean relative fluorescence intensity within the bleach spot, p is the Laplace variable that inverts to yield time, K_1 and I_1 are the first-order-modified Bessel functions of the first and second kind, respectively, w is the radius of the bleach spot, and k_{on} and k_{off} are the rate constants describing the rate of the cofactor binding-to and release-from the microbead surface, respectively. F_{eq} (eq 2) and C_{eq} (eq 3) represent the unbound and bound FAD concentrations at equilibrium, respectively. D_f (eq 4) is the diffusion coefficient of the cofactor in the absence of binding.

From the fitting of FRAP curves with eq 1, we derived k_{on} and k_{off} values and then calculated the ratio of k_{on}/k_{off}, which represents a pseudoequilibrium constant[38] that defines the population of bound and unbound FAD molecules inside one AG-Co^{2+}/E microbead coated with the polycations. FRAP studies demonstrate that a population of unbound FAD exists and can diffuse within the intraporal space of the microbeads without leaving them. According to their thermodynamic meanings, the higher the k_{on}/k_{off} values (FRAP dynamic curves), the higher the population of bound cofactors within the pores. Whereas the higher the K_D (in steady-state bulk experiments), the more cofactor molecules are unbound in the steady state. The inversely proportional relationship between k_{on}/k_{off} and K_D is clearly shown in Figure 3C. For instance, PEI binds FAD 6 times stronger than PAH in terms of steady-state binding (K_D), and consequently, the bound FAD population in PEI is 3 times larger than in PAH.

Hence, both bulk and single-particle studies support the fact that the polycationic coating is affecting both the steady-state thermodynamics and the population dynamics of the cofactor-bound/unbound equilibrium. Therefore, FRAP studies demonstrate that intraparticle FAD migration is affected by both the diffusion of the cofactor and its binding interactions toward the cationic coating. While some FAD molecules are bound to the cationic polymer, others freely diffuse through the pores of the carrier. As the ionic adsorptions of PLP and NAD(P)H are also mainly driven by their phosphate groups like FAD, we suggest that bound and unbound cofactor states are governed by a reversible equilibrium in all cases, and the magnitude of each population depends on the physicochemical properties of the cationic coating where they are adsorbed. This proven intraparticle cofactor migration allows the confined cofactor to access co-immobilized enzymes, although both enzyme and cofactor intraparticle localizations are unmatched (Figure 2).

Once demonstrated that phosphorylated cofactors can travel within the agarose porous microbeads coated with cationic polymers, we then confirmed that bound cofactors were barely lixiviated from their corresponding carriers after 8 washing steps (Figure S5). Thereby, phosphorylated cofactors can establish an intraporal association/dissociation equilibrium enabling their access to the active sites of the enzyme, thus activating the biocatalyst without diffusing out the microbeads. In addition, it was shown that cofactors were significantly more stable when they were adsorbed on AG-Co^{2+}/E-PEI compared to those in solution (Figure S6). For example, when NADH was adsorbed on AG-Co^{2+}/E-PEI preserved its maximum
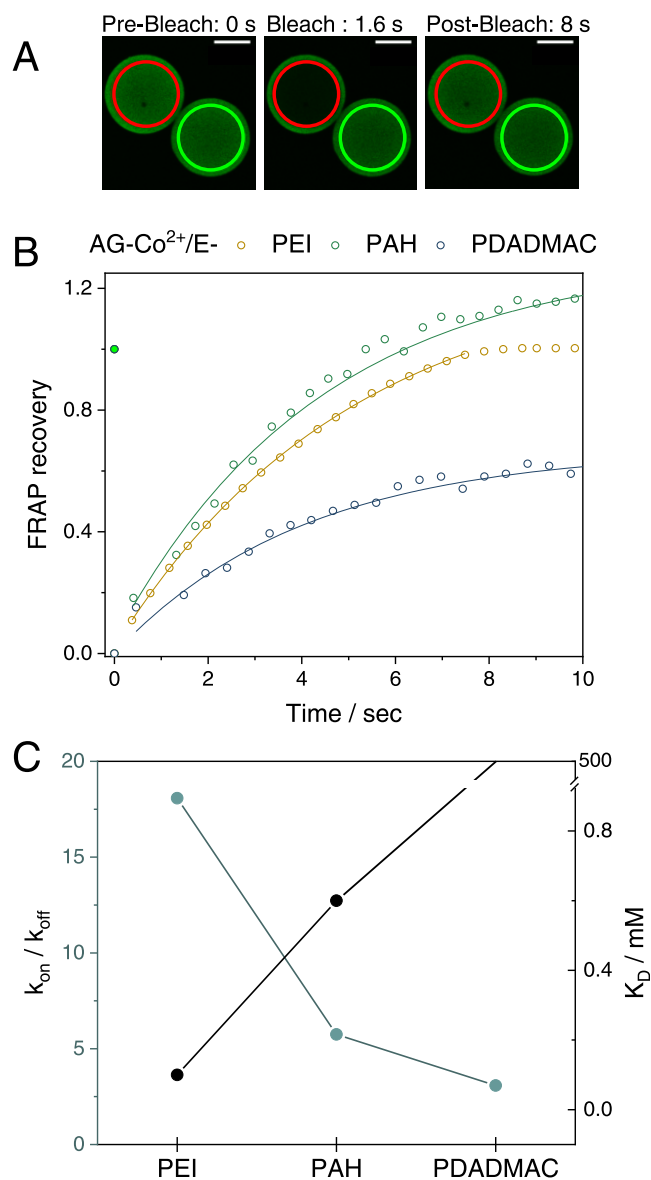

Figure 3. Fluorescence recovery after photobleaching (FRAP) analysis to study the intraparticle diffusion of cofactors. (A) Confocal fluorescence images before, during, and after photobleaching of the fluorescent FAD (green channel, λ_{ex}: 488 nm) adsorbed on AG-Co^{2+}/E carriers coated with PEI. The red circular region of interest (ROI, 93 μm) represents the photobleached area, and the green ROI represents the nonbleached area of the same size, used as a control. Scale bar, 50 μm. (B) FRAP normalized curves of FAD recovery when adsorbed to the different polycations PEI (yellow), PAH (green), and PDADMAC (blue). Dots represent the experimental data, while the solid line corresponds to the full reaction–diffusion model fitting (see the Materials and Methods section). (C) Pseudoequilibrium constant k_{on}/k_{off} calculated from FRAP analysis as a function of the dissociation constant K_D calculated from Langmuir adsorption Isotherms (Table 1). K_D data point for PDADMAC (not visible) is ≫500 according to its linear adsorption isotherm (see Figure S4).

absorbance peak at 340 nm after 4 days of storage at 4 °C, while the absorbance of the free cofactor disappeared after 1 day of storage, in accordance with previous findings.[43] Preservation of the optical properties of NADH when adsorbed on PEI-coated porous microbeads indicates that under the studied conditions, NADH maintains its chemical integrity and thus its biological activity.
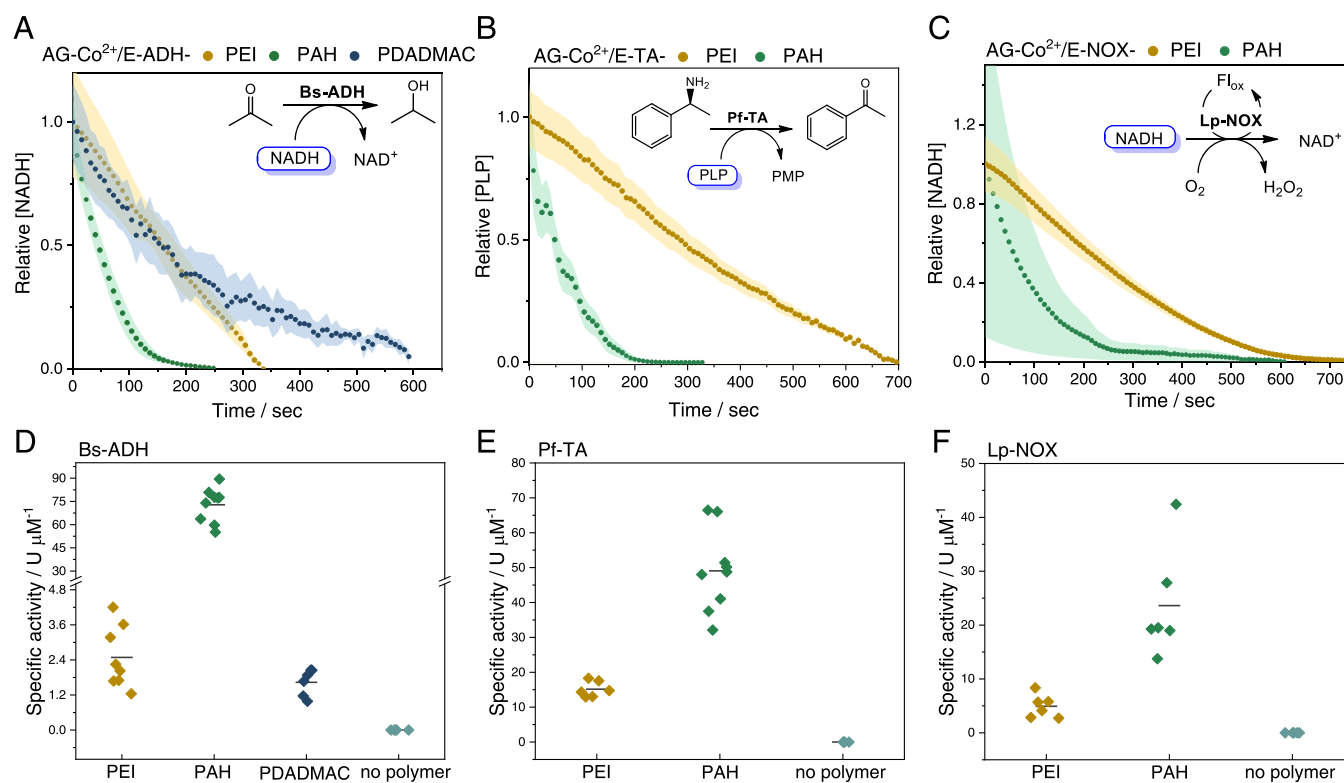
Figure 4. Single-particle activity of different enzyme/cofactor pairs co-immobilized on AG-Co^{2+}/E coated with different polycations: PEI (yellow), PAH (green), and PDADMAC (blue). (A–C) Single-particle normalized mean time courses of the relative cofactor concentration. Time data points are obtained from the mean value of 10 microbeads with the standard deviation depicted in shadows of the same color. (D–F) Single-particle specific activity of different immobilized systems. Each data point represents the specific activity of one single bead. Specific activity is defined as the activity units per enzyme concentration (U μM^{-1}). The activity unit (U) is defined as the concentration of the cofactor consumed per second (μM s^{-1}). (A and D) Bs-ADH co-immobilized with NADH using acetone as an exogenous substrate, (B and E) Pf-TA co-immobilized with PLP using rac-phenylethylamine as a substrate, and (C and F) Lp-NOX co-immobilized with NADH using riboflavin as a flavin cofactor. Insets (A–C) reaction schemes of each biocatalyst.

Kinetic Parameters of Enzymes Co-Immobilized with Their Phosphorylated Cofactors as Extracted from Single-Particle Analysis under *Operando* Conditions. We first studied the sample heterogeneity when different enzymes were co-immobilized with their corresponding cofactors using different cationic polymers. To that aim, we performed time-lapse fluorescence microscopy measurements and acquired single-particle time reaction courses, as described in the Materials and Methods section. This methodology allows us to analyze simultaneously single-particle enzyme kinetics of up to 20 beads that range from 50 to 150 μm, informing us about the functional heterogeneity of enzymes immobilized on carriers with broad particle size distributions. In addition, we can obtain intraparticle information of enzyme kinetics with a resolution of 1.6 μm px^{-1} that enabled us to generate functional radial profiles (*vide infra*). Figure 4A shows the mean time course of immobilized Bs-ADH oxidizing the confined NADH in the presence of exogenous acetone. Figure 4B shows the mean time course of the immobilized Pf-TA aminating the confined PLP in the presence of exogenous rac-1-phenylethylamine and the absence of amine acceptor (first half-cycle of the transamination reaction). Figure 4C shows the mean time course of the immobilized Lp-NOX oxidizing the confined NADH in the presence of exogenous riboflavin (Rf), a flavin cofactor required by the oxidase catalysis.[28] Each co-immobilized pair (enzyme/cofactor) exhibited different reaction rates depending on the polymer used for the

fabrication of the self-sufficient heterogeneous biocatalyst. In all cases, biocatalysts coated with PAH presented faster reaction time courses. A similar trend was also observed for the mean time courses of the immobilized Bs-KRED oxidizing the confined NADPH in the presence of dihydroxyacetone (Figure S7). When we calculated the specific activity of the immobilized rhodamine B (RhB)-labeled enzymes toward their confined cofactor (for details, see the Materials and Methods section) through single-particle analysis (Figure 4D–F), we identified three major facts. First, specific activities of co-immobilized enzyme/cofactor pairs were always greater than those obtained with immobilized enzymes with no coated polymer (cofactor not adsorbed) measured under the same microscopic activity assay. Such higher enzyme activities may rely on a mass action effect (concentration of reaction components) explained by the higher effective cofactor concentration in the surroundings of the immobilized enzymes when both enzyme and cofactor are co-immobilized. A similar observation has been reported elsewhere for trypsin immobilized on microfluidic nanochannels.[44]

Second, a remarkable dispersion of the specific activity values is observed among different microbeads coated with polymers regardless of the type of the enzyme. Such data dispersion reflects a functional heterogeneity of the immobilized enzymes within microbeads of similar size that is concealed in bulk experiments. Third, PAH coatings yield the most active self-sufficient heterogeneous biocatalysts
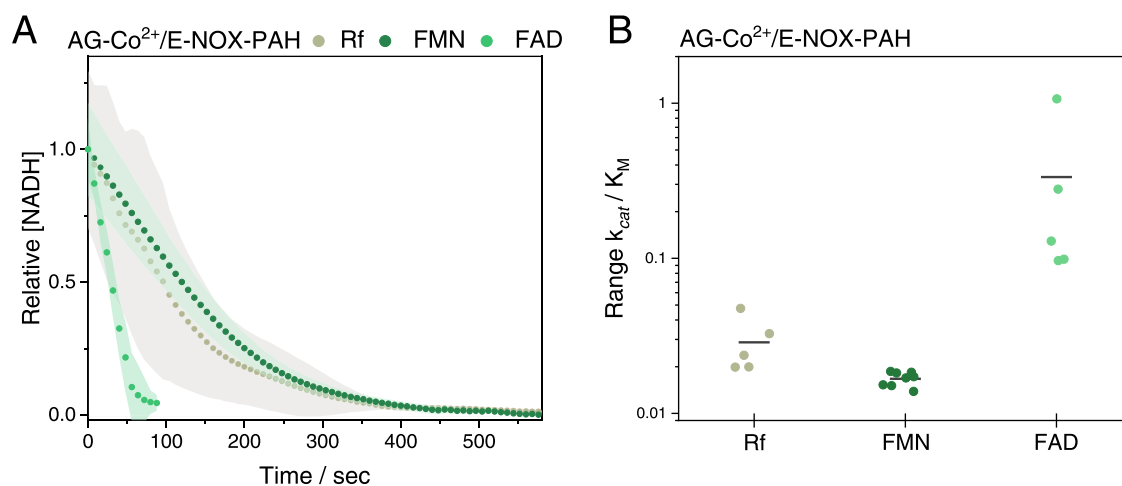
Figure 5. Single-particle reaction of Lp-NOX co-immobilized with NADH on AG-Co^{2+}/E-PAH in the presence of different flavins: riboflavin (Rf, gray), FMN (dark green), and FAD (light green). (A) Single-particle normalized mean time courses of the relative NADH concentration. Time data points are obtained from the mean value of 10 microbeads with the standard deviation depicted in shadows of the same color. (B) Apparent catalytic efficiency (k_{cat}/K_M) of Lp-NOX co-immobilized with NADH on AG-Co^{2+}/E-PAH in the presence of Rf, FMN, and FAD, as flavin cofactors. Each data point represents the apparent catalytic efficiency toward the confined NADH in one single bead.

regardless of the enzyme/cofactor co-immobilized pair, supporting the hypothesis that an optimal bound/unbound equilibrium of the cofactor enhances its intraporal diffusion to reach the active sites of the immobilized enzymes more effectively. Although not investigated here, the herein used polymers may induce stabilizing/destabilizing effects on the immobilized enzymes upon the coating step. Interestingly, it has been reported that enzymes bound to weak polyelectrolytes (i.e., PAH) suffer less structural distortions and thus are more active than those bound to strong ones (i.e., PDADMAC).[45] Therefore, differences found in the specific activity of the same immobilized enzyme but coated with different cationic polymers are due to a combination of factors (cofactor diffusion and enzyme stability).

Intrigued by these differences, we determined the apparent MM parameters of Lp-NOX co-immobilized with NADH on AG-Co^{2+}/E-PAH since the activity of this heterogeneous biocatalyst can be triggered by the addition of different flavins,[28] phosphorylated or not. Time courses (Figure 5A) were recorded in single-particle experiments in the presence of Rf, flavin mononucleotide sodium salt (FMN), or FAD to determine the corresponding apparent kinetics. The reaction courses were then fitted to the closed-form solution of the Michaelis–Menten equation[46] expressed by the Lambert W-function[47,48] to obtain the apparent kinetic parameters of the immobilized enzymes toward the adsorbed cofactors: K_M, k_{cat}, and apparent k_{cat}/K_M. Representative fittings of the closed-form solution of the MM equation expressed with the Lambert W-function are shown in Figure S8. The efficiency of the fittings was also evaluated in terms of R^2, which was greater than 0.99 in all cases. Figure 5B shows that the apparent catalytic efficiency (k_{cat}/K_M) of the immobilized Lp-NOX toward the confined NADH significantly varies with the type of flavin added to the reaction bulk.

In the presence of FAD, Lp-NOX presents a 10-fold higher apparent k_{cat}/K_M than in the presence of Rf or FMN. Single-particle studies confirmed that Lp-NOX is poorly active in the absence of any exogenous flavin, as reported elsewhere.[28] Unlike Rf, which lacks phosphate groups, FAD and FMN were co-adsorbed with NADH on the PAH coating during the

reaction course. Our group has recently reported a similar co-immobilization pattern using a NOX from *Thermus thermophilus* HB27 immobilized on agarose microbeads functionalized with aldehyde groups and coated with PEI;[49] however, single-particle experiments were not performed. Therefore, FAD and FMN were confined into the same porous microbead together with the substrate (NADH) and the enzyme. In this scenario, the interactions between the flavins and the carrier seem to affect their microscopic interplay with the immobilized Lp-NOX, driving to heterogeneous biocatalysts with different performances. We suggest that the differences found in the apparent kinetics of the immobilized enzymes when using different flavins are due to two main factors: (1) different K_M values for the molecular complex Lp-NOX-flavin and (2) different binding thermodynamics (K_D) between the flavin and the polycationic coating inside the self-sufficient heterogeneous biocatalyst. To confirm the role of these two factors, we determined the K_M of soluble Lp-NOX toward FMN and FAD in bulk, as well as the K_D of these flavins ionically absorbed on AG-Co^{2+}/E-PAH carriers (for details, see the Materials and Methods section). Free Lp-NOX exhibits a 5-fold lower K_M toward FAD ($K_M = 0.041 \pm 0.02$ mM) than toward FMN ($K_M = 0.215 \pm 0.1$ mM), (Figure S9), while the binding thermodynamics points out that FAD is 4 times less strongly adsorbed ($K_D = 0.6$ mM) to PAH than FMN ($K_D = 0.14$ mM), (Figure S10). Hence, the enhanced catalytic efficiency of the immobilized Lp-NOX on AG-Co^{2+}/E-PAH toward the confined NADH is explained by the higher intrinsic affinity of such enzyme toward FAD (lower K_M) and the larger unbound FAD population (higher K_D) that becomes more available for the immobilized enzyme, compared to FMN.

Particle-to-Particle Kinetic Variability of Immobilized Enzymes under *Operando* Conditions. The functional dispersion among beads found in Figures 4 and 5 encouraged us to investigate the particle-to-particle functional dispersion in commercial carriers like agarose porous microbeads.[23] Through monitoring single-particle reaction courses, we study the effects of protein concentration on the apparent kinetic parameters of immobilized enzymes toward their confined cofactors. As a model system for these studies, we
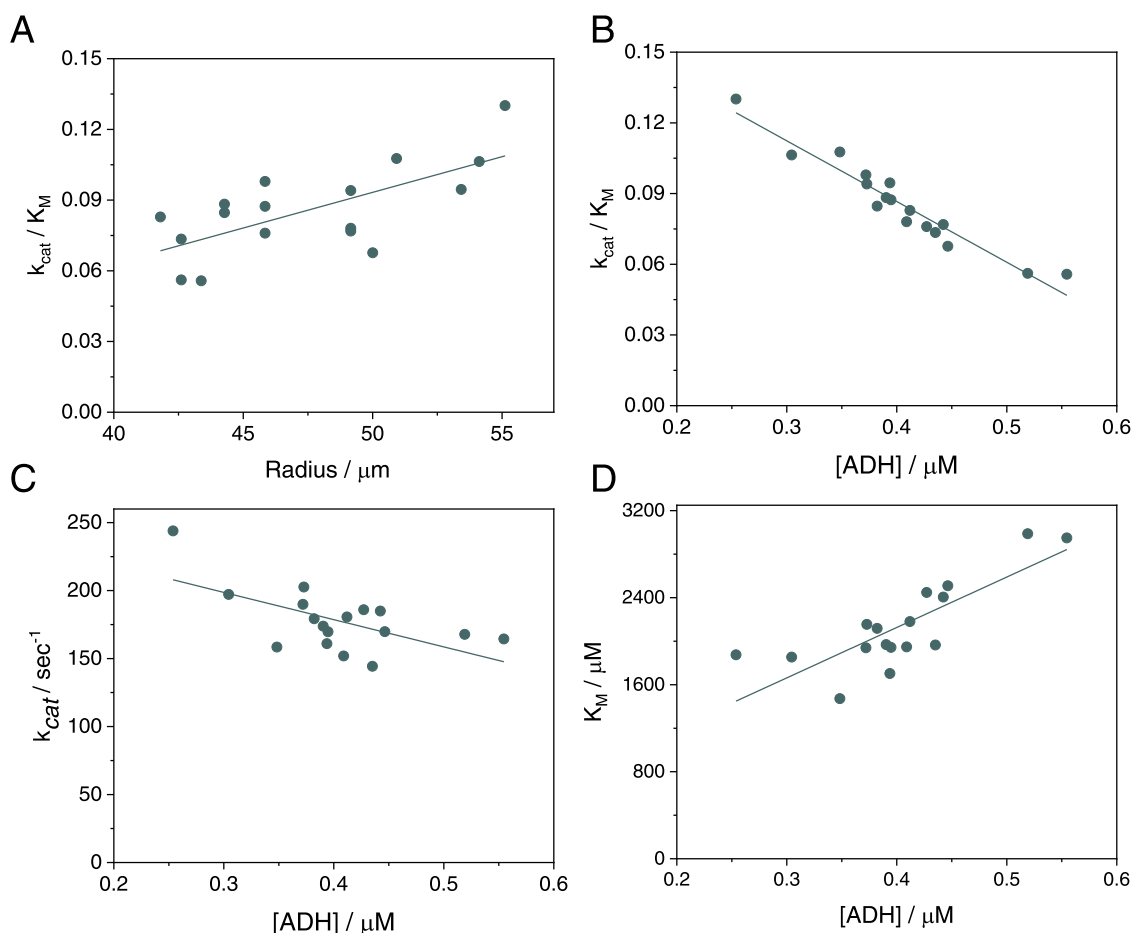
Figure 6. Effect of microbead radius and enzyme concentration on the apparent Michaelis−Menten kinetics of Bs-ADH co-immobilized with NADH on AG-Co^{2+}/E-PAH. (A) Apparent k_{cat}/K_M toward NADH as a function of the microbead radius. (B) Apparent k_{cat}/K_M toward NADH as a function of the enzyme concentration immobilized on one single microbead. (C) Apparent k_{cat} and (D) apparent K_M toward NADH versus the concentration of immobilized Bs-ADH. Each data point represents the corresponding apparent kinetic parameter toward the confined NADH in one single microbead. For statistical measurements, we performed linear regression (OriginLab) on each scatterplot and analysis of variance (ANOVA) statistical analysis to derive Pearson's correlation coefficient (r) and P-values, respectively. Statistical analysis of (A), (B), (C), and (D) resulted in $r = 0.7$ ($p < 0.005$), $r = −0.9$ ($p < 0.005$), $r = −0.6$ ($p < 0.005$), and $r = 0.8$ ($p < 0.005$), respectively.

selected RhB-labeled Bs-ADH co-immobilized with NADH on AG-Co^{2+}/E-PAH microbeads with particle radius size ranging from 40 to 60 μm. Despite this narrow range, we still observed that the V_o of immobilized Bs-ADH slightly decreased as the particle size increased (Figure S11A). This is consistent with the previous bulk[48] and single-particle studies[23] that show similar effects. Remarkably, the immobilized Bs-ADH concentration negatively correlated with the particle radius; therefore, smaller microbeads loaded higher enzyme concentrations, resulting in higher single-particle initial rates (V_o) (Figure S11B). Such variability was also observed for other enzymes, where higher protein loadings were obtained using small particles as carriers.[22,50] When apparent kinetics were extracted from single-particle reaction courses, we found that, unlike V_o, the apparent k_{cat}/K_M values slightly increased with the particle radius, displaying a weak positive correlation (Figure 6A). In contrast, the apparent k_{cat}/K_M had a strong negative correlation with the intraparticle enzyme concentration (Figure 6B), indicating that the highest apparent k_{cat}/K_M values correspond to the particles with the lowest enzyme concentrations. Interestingly, we observed that K_M of immobilized Bs-ADH toward the co-immobilized NADH showed a positive correlation with the intraparticle enzyme concentration

compared to k_{cat} values that show a weaker negative correlation (Figure 6C,D). Such correlation differences indicate that the apparent K_M affected the apparent k_{cat}/K_M to a larger extent than the apparent k_{cat}. Hence, Bs-ADH molecules immobilized on particles with high protein densities (high intraparticle enzyme concentration) exhibit lower apparent catalytic efficiencies due to their higher apparent K_M values. Moreover, the intraparticle NADH concentration negligibly affected the apparent catalytic efficiency (Figure S12), suggesting that the co-immobilized enzymes are saturated with NADH although its intraparticle concentration (3937 ± 233 μM) slightly varies from bead to bead. In the light of these data, we suggest that the apparent catalytic efficiency of the immobilized enzyme is mainly affected by the intraparticle enzyme concentration. Our suggestion is supported by bulk activity measurements at different free Bs-ADH concentrations under the same conditions as single-particle experiments, demonstrating that the specific activity of the free enzyme decreases as the enzyme concentration increases (Figure S13A).

Additionally, when we determined the kinetic parameters of the soluble Bs-ADH toward soluble NADH under the same conditions (excess of acetone) (Figure S13B), we found that the apparent K_M value (67.4 ± 22 μM) was 2 orders of
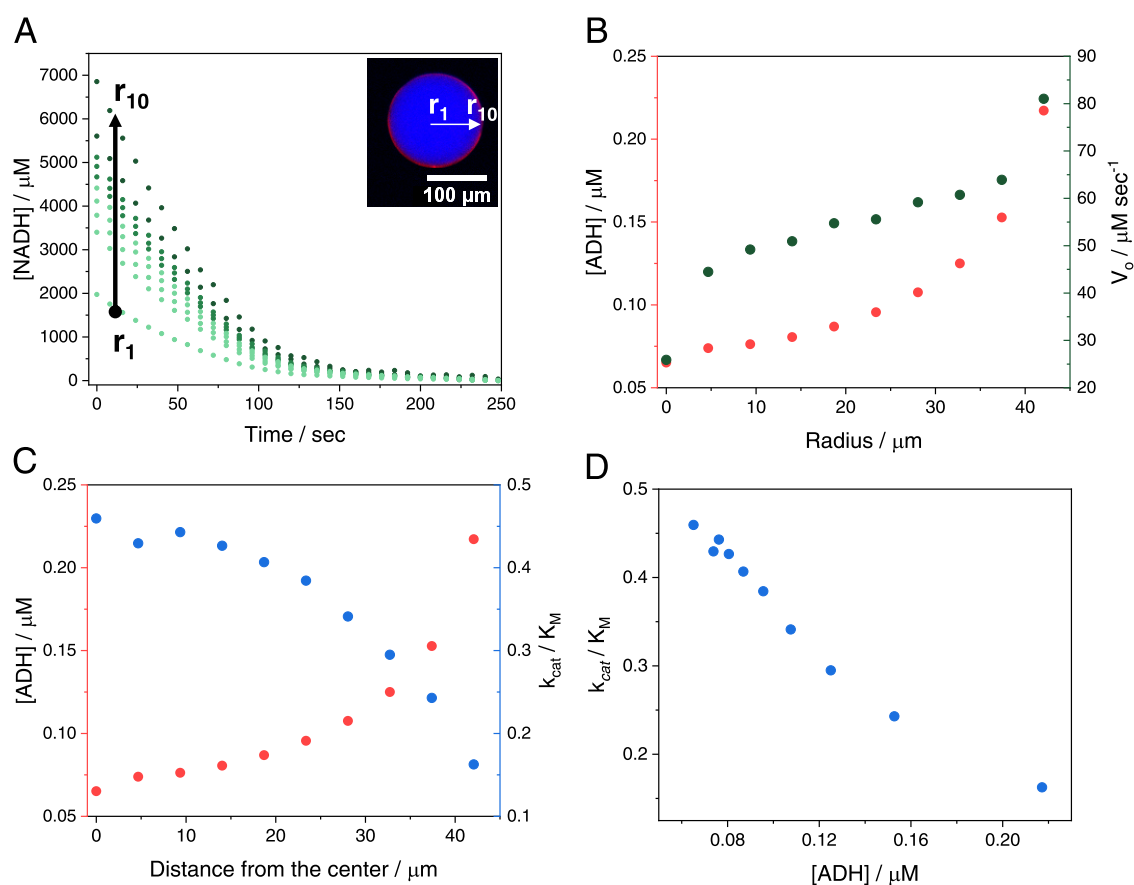
Figure 7. Intraparticle kinetic studies of Bs-ADH co-immobilized with NADH on AG-Co^{2+}/E-PAH. (A) Intraparticle time courses of NADH oxidation in the presence of acetone at different positions of the radial intensity profile (r_1: center, r_{10}: outer surface of one single microbead). Top right inset: representation of the radial intensity profile in the merged fluorescence image of RhB-labeled Bs-ADH (red channel, λ_{ex}: 523 nm) co-immobilized with fluorescent NADH (blue channel, λ_{ex}: 365 nm). (B) Intraparticle enzyme concentration (left y-axis) and initial rate V_o (right y-axis) measured at different positions of the radial intensity profile. (C) Intraparticle enzyme concentration (left y-axis) and apparent k_{cat}/K_M (right y-axis) as determined from the time courses in panel (A) at different distances from the center of the microbead. (D) Intraparticle apparent k_{cat}/K_M as a function of the local Bs-ADH concentration within one single microbead.

magnitude lower than the value calculated for the immobilized enzyme toward the confined cofactor, which ranges between 1500 and 3200 μM depending on the intraparticle enzyme concentration. This insight into the microscopic level aligns with the data obtained from bulk studies, where immobilized biocatalysts loaded with high protein densities exhibit higher apparent K_M values[51,52] than those with lower loads. Hence, the dependency of enzyme kinetics with the concentration of the immobilized enzyme suggests that immobilized Bs-ADH undergoes crowding effects that alter its functionality. Similar crowding effects were observed for the Pf-TA co-immobilized with PLP, whose apparent catalytic efficiency decreased as the enzyme concentration increased (Figure S14A). The effect of molecular crowding on enzyme kinetics has been studied *in vitro* (using artificial crowders) for several free enzymes.[53,54] However, crowding effects are less often described for immobilized enzymes. Although exogenous molecules and confined cofactors present much smaller sizes than the immobilized enzymes, molecular crowding within the microbeads may create excluded volume effects[53] that reduce the diffusion rates of both the immobilized cofactor and the exogenous substrate toward the active sites of the immobilized enzymes, thus affecting their apparent kinetics. In contrast, the intraparticle concentration of Lp-NOX poorly correlated with its catalytic efficiency toward NADH in the presence of

exogenous riboflavin (Figure S14B). Taking into account that immobilized NADH oxidases undergo oxygen and cofactor transport limitations,[49] we suggest that the Lp-NOX performance is affected more by the limiting exogenous concentration of both oxygen and flavin (0.15−0.2 mM) than by the enzyme density within the particles. This fact thus explains the lack of correlation between Lp-NOX kinetics and intraparticle enzyme concentration, unlike what we observed with Bs-ADH and Pf-TA.

Thus, sample heterogeneity unveiled by *in operando* single-particle experiments indicates the existence of several particle populations where the immobilized enzymes act under different crowding conditions. These data aid in explaining the functional dispersity of the samples, despite being measured under the same reaction conditions (pH, temperature, and substrate concentration).

Spatial Resolution of Intraparticle Apparent Kinetics for Immobilized Enzymes under *Operando* Conditions. Heterogeneity in enzyme apparent kinetics toward the co-immobilized cofactor was further explored through intraparticle analysis at a micrometric level (spatial resolution of 1.67 μm px^{-1}) within one single microbead of AG-Co^{2+}/E-PAH where RhB-labeled Bs-ADH and NADH were co-immobilized. We derived intraparticle functional radial profiles across the orthographic projection (2D image) of one single
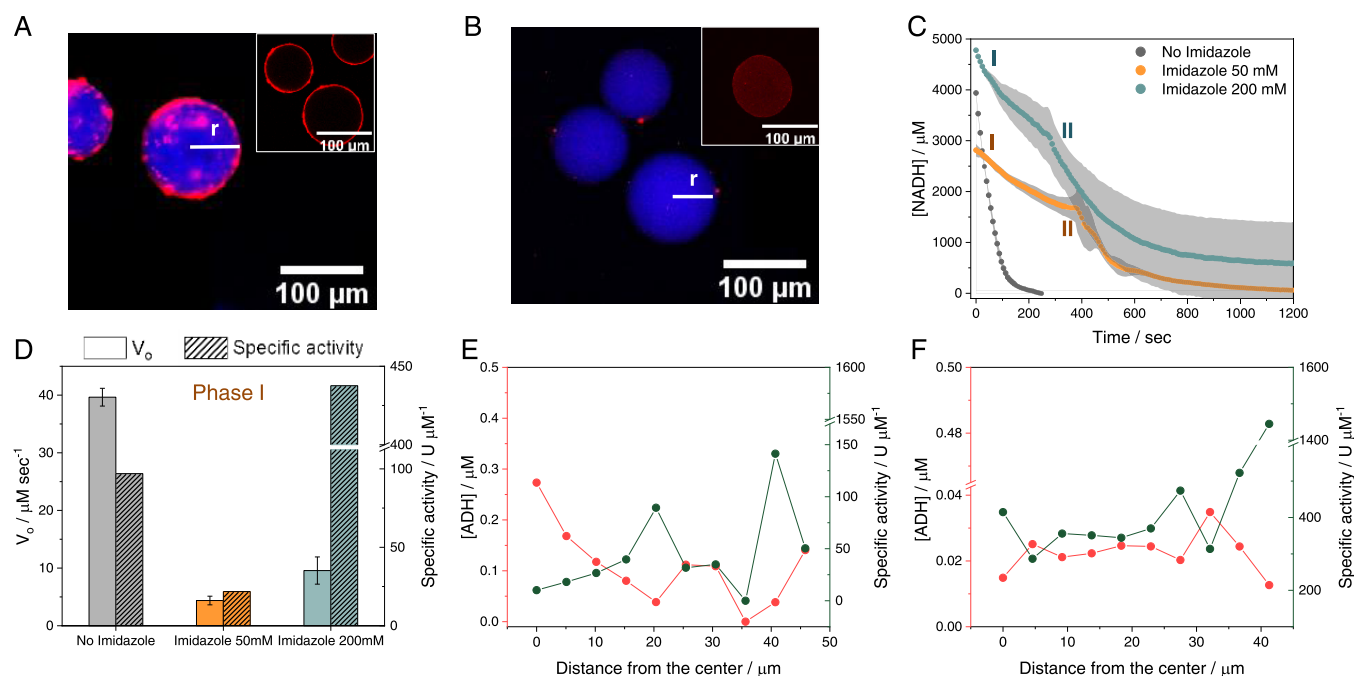
Figure 8. Effect of spatial distribution on the single-particle and intraparticle kinetics of Bs-ADH co-immobilized with NADH on AG-Co^{2+}/E-PAH. (A and B) Epifluorescence and confocal fluorescence (top right inset) merged images of RhB-labeled Bs-ADH (red channel, λ_{ex}: 523 nm) immobilized with different spatial distributions, and co-immobilized with fluorescent NADH (blue channel, λ_{ex}: 365 nm) on AG-Co^{2+}/E-PAH carriers. (A) Bs-ADH immobilization in the presence of 50 mM imidazole resulting in patches at the outer surface of the microbead and (B) Bs-ADH immobilization in the presence of 200 mM imidazole resulting in a uniform distribution across the microbead, where r (white line) depicts the radial intensity profile position of one selected microbead. (C) Single-particle time courses of NADH oxidation in the presence of acetone using immobilized systems with different Bs-ADH spatial distributions; no imidazole (gray, see Figure 6A), imidazole 50 mM (yellow), and 200 mM imidazole (blue). Time data points are obtained from the mean value of 10 microbeads with the standard deviation depicted in shadows of the same color. The first and second phases of the biphasic time courses are represented with symbols I and II, respectively. (D) Initial rate and enzyme-specific activity calculated from Phase I of the time courses shown in panel C for each immobilized enzyme with the different spatial distribution. Specific activity is defined as the activity units per enzyme concentration (U μM^{-1}). The activity unit (U) is defined as the concentration of the cofactor consumed per second (μM s^{-1}). (E) Radial intensity profiles of the intraparticle enzyme concentration and intraparticle specific activity within one single microbead of the self-sufficient heterogeneous biocatalyst prepared in the presence of 50 mM imidazole. (F) Radial intensity profiles of the intraparticle enzyme concentration and intraparticle specific activity within one single microbead of the self-sufficient heterogeneous biocatalyst prepared in the presence of 200 mM imidazole.

microbead and obtained a pool of time courses in 10 intraparticle radial intensity positions separated by a distance equal to 10% of the radius (Figure 7A) (for details, see the Materials and Methods section). Briefly, in a particle of 50 μm radius, r_5 is the average of the time courses corresponding to all pixels located at 25 μm from the center of the microbead (inset, Figure 7A). The shape of the time courses varied depending on the coordinate of the radius where they were recorded. Using the image analytics tool described in the Materials and Methods section together with the volumetric correction previously developed in our group,[23] we were able to locally estimate the apparent kinetic parameters of the immobilized enzymes toward the confined cofactor in areas as small as 2.8 μm^2. Furthermore, we calculated the enzyme concentration immobilized on those small areas. Having the local reaction progress and enzyme concentrations, we determined the variability of the initial rate and the apparent MM kinetics along with the radial intensity profile of one single microbead. The concentration profile of Bs-ADH obtained from the corresponding intensity radial profiles confirms that the enzyme mainly colonized the outer 14 μm of the AG-Co^{2+}/E-PAH microbeads. As expected, we found that the highest initial rates were at the outermost particle regions, where we found the highest enzyme concentration (Figure 7B). Moreover, in those regions, the diffusion distance

that the exogenous substrate (acetone) must travel to reach the active sites of the enzymes is shorter. On the contrary, we observed significantly higher apparent k_{cat}/K_M values at the inner regions of the particle for this self-sufficient heterogeneous biocatalyst (Figure 7C). When the catalytic efficiency was plotted versus the enzyme concentration (Figure 7D), we observed how the former inversely scales with the latter. Therefore, intraparticle kinetics confirm the relationship between the activity and density of the immobilized enzyme as observed through singe-particle analysis (Figure 6) and studies in solution (Figure S13A). Hence, we suggest that molecular crowding effects reduce the catalytic efficiency of Bs-ADH, most likely due to the decrease of the intraparticle diffusion rates of both substrate and cofactors, but may also alter protein conformational dynamics as proven for other types of enzymes measured in the presence of artificial crowders.[55] Further studies are needed to demonstrate changes in dynamics due to the crowding of Bs-ADH molecules at the surface of porous agarose microbeads. These changes have been simulated and experimentally demonstrated in dense media and planar surfaces;[56−58] nevertheless, the effects of crowding on dynamics of proteins confined into porous materials are poorly understood.

Effect of Enzyme Spatial Distribution on Intraparticle Apparent Kinetics under *Operando* Conditions. The

variability of enzyme functionality within the same particle and its relationship with both the local concentration and localization of the immobilized enzymes encouraged us to study how different enzyme spatial distributions affected the kinetic properties of the final heterogeneous biocatalyst. We first prepared different self-sufficient heterogeneous biocatalysts having different spatial distributions of Bs-ADH across the porous surface of AG-Co^{2+}/E-PAH. The spatial organization of the enzymes within the porous microbeads was controlled by adding immobilization competitors that slow down the immobilization process, thus avoiding their massive immobilization on the outer surface and facilitating their infiltration toward inner regions of the particles.[59] In the absence of inhibitors, the binding reaction kinetics between the enzyme and the carrier govern the immobilization process, while in the presence of inhibitors, the enzyme diffusion across the carrier dominates the immobilization process. This control is useful to fabricate heterogeneous biocatalysts where enzymes are either nonuniformly or uniformly distributed across the carrier surface.[49,59,60] In the case we study, the immobilization of His-tagged Bs-ADH was performed at different imidazole concentrations (50 and 200 mM) that competed with the His-tag for their binding to the cobalt chelates at the carrier surface, allowing the enzyme to colonize the inner surface of the carrier. Then, NADH was ionically adsorbed on AG-Co^{2+}/E-PAH carriers with different spatial organizations of the immobilized Bs-ADH. As expected, NADH was always uniformly distributed, while the localization of Bs-ADH depended on the imidazole concentration used during the immobilization process (Figure 8A,B). In the case of 50 mM imidazole, CLSM images revealed that Bs-ADH was randomly localized in clusters at the outer regions of the microbeads (inset, Figure 8A). This spatial organization was not observed for the immobilization in the absence of imidazole, where the enzyme was homogeneously distributed at the outer 14 μm of the microbeads (inset Figure 7A). In the case of 200 mM imidazole, Bs-ADH was uniformly immobilized across the entire microbead surface (inset, Figure 8B) and fully colocalized with the confined NADH. The averaged single-particle reaction time courses showed significant differences in curve shapes depending on the Bs-ADH spatial organization (Figure 8C). Unlike the hyperbolic curves obtained when the enzyme was mainly located at the outer surface of the microbeads, single-particle reaction time courses were biphasic when Bs-ADH was immobilized in the presence of imidazole, according to principal component analysis (PCA) (for details, see the Materials and Methods section). In the obtained biphasic curves, we could identify two linear slopes that corresponded to different initial reaction rates, suggesting that the obtained activity was of at least two enzyme populations (within the microbeads) that may work under two different apparent kinetic regimes. Unfortunately, our analysis was only based on the initial rate data as the Michaelis−Menten equation expressed by the Lambert W-function failed to fit the biphasic time courses; therefore, we were unable to estimate the apparent MM kinetic parameters for the two different reaction phases. Figure 8D shows the average single-particle initial rates measured for Bs-ADH immobilized through different spatial distributions. Here, we observed that when Bs-ADH was localized at the outer surface of the carrier (the absence of imidazole), the initial rate was 5−10 times higher than the obtained initial rates (phase I) when Bs-ADH was either uniformly distributed across (200 mM imidazole) or was

forming dense enzyme patches at the outer surface of the microbeads (50 mM imidazole), respectively. When the initial rates of phase I were divided by the intraparticle enzyme concentration (enzyme-specific activity), we observed that the spatial organization of Bs-ADH affected its catalytic performance due to different enzyme concentration distribution across the microbead. Despite having the lowest overall reaction rates, the particles where the enzymes were quite uniformly distributed (immobilization with 200 mM imidazole) exhibited a specific activity 4.5 times higher than the enzymes localized at the outermost regions of the particles (immobilization with no imidazole). In contrast, particles that contained enzyme patches with high local protein concentration exhibited a specific activity 20 times lower than the ones observed for the enzymes uniformly distributed across the whole microbead. Similar trends were observed for the specific activities derived from initial rates of phase II (Figure S15).

To better understand these complex biochemical processes in the confined space, we studied the specific activity gradients at different positions of the microbead that corresponded to different enzyme concentrations. *In operando* microscopic analysis allowed us to create radius profiles for the intraparticle concentration and the specific activity of Bs-ADH immobilized in the presence of 50 mM (Figure 8E) and 200 mM (Figure 8F) of imidazole. Intraparticle profiles shown in Figure 7C demonstrated that the regions allocating higher local enzyme concentrations exhibited lower catalytic efficiency. This fact was manifested more clearly when Bs-ADH was randomly immobilized in patches within one single microbead. Regions with low activity corresponded to highly enzyme populated regions, resulting in microbeads with jagged profiles along the particle radius for both enzyme concentration and specific activity (Figure 8E). On the contrary, in those microbeads where the enzymes were uniformly distributed across their surface, their profiles were flatter (Figure 8F), suggesting that enzymes work evenly across the radius profile only when enzymes are highly diluted across the whole microbead surface. Therefore, intraparticle analysis demonstrated that functional variability is observed not only between different microbeads but also between different regions within the same microbead. Both inter and intraparticle studies proved that the apparent kinetics of Bs-ADH co-immobilized with NADH rely on the local enzyme concentrations, supporting the fact that crowding environments negatively affect the performance of this enzyme. Besides the mass transport issues suggested by the single-particle apparent kinetics, intraparticle kinetic analysis elicited that low apparent specific activity of highly crowded regions is due to the high local molar ratio between the enzyme and the cofactor, implying that the enzymes localized in those regions work under cofactor limiting conditions (first-order reaction law). Hence, molecular crowding of enzymes seems to exacerbate other effects at both molecular (conformational dynamics) and system levels (mass transport restrictions) that ultimately limit the apparent enzyme activity.

Therefore, single-particle and intraparticle kinetic studies unmask the localization and density of the immobilized enzymes as key factors to enhance the kinetic properties of heterogeneous biocatalysts. Hence, we anticipate the spatial distribution of enzymes immobilized on solid materials as a fundamental parameter to be optimized during the fabrication of more efficient and robust heterogeneous biocatalysts with advanced properties. In the last few years, our group, among others, accomplished to enhance the activity of immobilized

enzymes by controlling their spatial distribution;[61] however, these heterogeneous biocatalysts need to be further characterized through multiscale *in operando* methods to achieve a deeper understanding of the molecular and systemic reasons behind the observed improvements.

CONCLUSIONS

Single-particle analysis based on the processing of time-lapse fluorescence microscopy images allows us to comprehend the factors that rule out the intraparticle apparent kinetics of self-sufficient heterogeneous biocatalysts. To that aim, enzymes and their corresponding phosphorylated cofactors were co-immobilized but microscopically segregated within the same agarose microbead. Steady-state and single-particle thermodynamics demonstrated that the adsorption of phosphorylated cofactors on porous carriers coated with cationic polymers is governed by an association/dissociation equilibrium. Such equilibrium enables the intraparticle shuttling of phosphorylated cofactors to access the active site of the co-immobilized enzymes without leaving the carrier volume, even after several washing steps. This association/dissociation equilibrium relies on the physicochemical features of the polycation coatings and demonstrates that the cofactors can access the active site of their corresponding co-immobilized enzymes, although their intraparticle localizations are unmatched. Furthermore, we investigated the effect of local enzyme concentrations on the intraparticle apparent MM kinetics of the immobilized enzymes. This parameter was manifested as one of the major sources of functional variability for the self-sufficient immobilized biocatalysts. Finally, micrometric kinetic analysis with spatiotemporal resolution elicits the effects of spatial organization and molecular crowding on the enzyme performance. We demonstrated that lower enzyme densities localized at the outermost regions of the particles are the most productive conditions for the performance of the heterogeneous biocatalysts. Hence, we proved the usefulness of single-particle experiments to identify crowding effects with spatial resolution within porous microbeads, where proteins are nonuniformly distributed across their surface. All of these studies together provide essential information to understand the interplay between enzymes and cofactors within the confined space of porous materials and inform us about the particle-to-particle functional heterogeneity of macroscopic samples. We envision this multiscale characterization as an instrumental tool to better understand the *in operando* functionality of enzymes within confined spaces and the effects of the carrier surface on their properties, expanding the palette of parameters to be analyzed. The information that we elicit from our studies will contribute to develop more rational, reliable, and reproducible proceedings when fabricating heterogeneous biocatalysts.

MATERIALS AND METHODS

Materials. Agarose microbeads (50−150 μm diameter) were purchased from Agarose Bead Technologies (Madrid, Spain). Polyethyleneimine (PEI) solution in H_2O ($M_w \sim$ 60 000, 50 wt %), polyallylamine (PAH) solution in H_2O ($M_w \sim$ 65 000, 10 wt %), polydiallyldimethylammonium chloride (PDADMAC) solution in H_2O ($M_w <$ 100 000, 35 wt %), pyridoxal 5′-phosphate hydrate (PLP, 98%), rhodamine B isothiocyanate mixed isomers (RhB), acetone, 2-phenylethylamine (PEA, 98%), iminodiacetic acid (IDA), albumin bovine serum standard (BSA), and other reagents and solvents of analytical grade were purchased from Sigma-Aldrich (St. Louis, IL). Nicotinamide adenine dinucleotide-reduced sodium salt (NADH) and flavin mononucleotide sodium salt (FMN) were purchased from GERBU Biotechnik GmbH (Heidelberg, Germany). Flavin Adenine dinucleotide disodium salt hydrate (FAD, 94%) was purchased from Cymit Quimica S.L. (Barcelona, Spain). Riboflavin (Rf, 98%) was purchased from Acros Organics B.V.B.A. (Fair Lawn, New Jersey, United States). Isopropyl-β-D-thiogalactopiranoside (IPTG, 100%) was purchased from Fisher Bioreagents. The Bradford protein assay dye reagent was purchased from BIORAD (Biorad. Hercules, CA). Clear bottom black and white microplates (96-well) were purchased from Avantor (2021 VWR International, LLC). μ-Slides 8 well glass bottom was purchased from Ibidi (Planegg, Germany).

Enzyme Expression and Purification. Alcohol dehydrogenase from *B. stearothermophilus* (Bs-ADH), NADH oxidase from *L. pentosus* (Lp-NOX), ketoreductase from *B. subtilis* (Bs-KRED), and transaminase from *Pseudomonas fluorescens* (Pf-TA) with a 6-His-tag at the N-terminus were heterogeneously expressed in *Escherichia coli*. The genes encoding all enzymes were optimized for *E. coli* codon usages and synthesized by Genscript Biotech (Piscataway, NJ). The synthetic genes were cloned into pET28b(+) using *Nde*I and *Xho*I restriction sites. DNA isolation, plasmid purification, restriction analysis, plasmid construction, and DNA sequencing were carried out by standard methods.[62] Briefly, the recombinant plasmids that harbor the gene that encodes Bs-ADH, Lp-NOX, Bs-KRED, or Pf-TA were transformed into *E. coli* BL21 (DE3) chemically competent cells and cultivated under gently shaking at 37 °C in 50 mL of LB medium supplemented with 30 μg mL^{-1} of kanamycin until the OD 600 nm reached 0.4−0.6. At that point, the culture was induced with 1 mM IPTG for Bs-ADH and Lp-NOX expression and 0.1 mM IPTG for Pf-TA and Bs-KRED expression. After induction, the cells were grown at 37 °C for 3 h in the case of Bs-ADH and at 21 °C for 16 h in the cases of Lp-NOX, Bs-KRED, and Pf-TA. Finally, the cells were harvested by centrifugation at 4000*g* for 30 min at 4 °C. Then, the cell pellets containing Bs-ADH and Lp-NOX were resuspended in 25 mM sodium phosphate buffer at pH 7 containing 50 mM NaCl and 10 mM imidazole, Pf-TA was resuspended in 50 mM Tris−HCl buffer at pH 8 containing 100 mM NaCl, 30 mM imidazole, and 0.1 mM PLP, and Bs-KRED was resuspended in 50 mM sodium phosphate buffer at pH 7 containing 500 mM NaCl. The resulting suspensions were sonicated and centrifuged, and the supernatant containing the enzyme was purified by immobilized metal affinity chromatography (IMAC). All enzymes were eluted with elution buffer (50 mM Tris−HCl buffer containing 500 mM imidazole at pH 8). For Bs-KRED, the elution buffer also contained 500 mM NaCl, while the elution buffer for Pf-TA contained 0.1 mM PLP. Eluted proteins were then filtered in a tangential ultrafiltration unit (10 kDa) to remove imidazole and exchange the buffer with 25 mM sodium phosphate-buffered solution at pH 7 (and 0.1 mM PLP in the case of Pf-TA).

Enzymatic Activity Measurements in Solution (Bulk Measurements). Enzyme activities in solution were spectrophotometrically measured in a 96-well transparent microplate employing a Microplate Reader Epoch 2, BioTek, and activity values were derived using Gen5 software.

Bs-ADH Colorimetric Assay in Solution. The specific activity of soluble Bs-ADH was determined through colorimetric assay measurements. More specifically, 200 μL of a reaction mixture containing 64 mM acetone and 0.1−1 mM NADH in 25 mM phosphate buffer at pH 7 was incubated with 5 μL of a free enzyme at 30 °C. The decrease in absorbance was monitored at 340 nm. One unit of activity was defined as the amount of enzyme that was required to oxidize 1 μmol of NADH per minute at the assayed conditions. To calculate the Michaelis−Menten constant (K_M) toward NADH, the enzyme activity (U) was divided by the enzyme concentration and these values were plotted against the NADH concentration. Finally, the experimental data were fitted to the Michaelis−Menten equation using OriginLab software.

Lp-NOX Colorimetric Assay in Solution. The specific activity of soluble Lp-NOX was determined through colorimetric assay measurements. More specifically, 200 μL of a reaction mixture containing 0.2 mM NADH and 0.025−0.2 mM of either FMN or FAD in 25 mM phosphate buffer at pH 7 was incubated with 10 μL of suspension (1:10) of the different biocatalysts at 30 °C. The decrease in absorbance was monitored at 340 nm. One unit of activity was defined as the amount of enzyme that was required to oxidize 1 μmol of NADH per minute at the assayed conditions. To calculate the Michaelis−Menten constant (K_M) toward either FMN or FAD, the enzyme activity (U) was divided by the enzyme concentration and these values were plotted against the flavin cofactor concentration. Finally, the experimental data were fitted to the Michaelis−Menten equation using OriginLab software.

Enzyme Fluorescence Labeling. Fluorescence labeling of Bs-ADH, Lp-NOX, and Pf-TA with rhodamine B (RhB) was carried out as described elsewhere.[60] Briefly, the enzyme in 100 mM sodium bicarbonate buffered solution at pH 8.5 was mixed with RhB solution in DMSO (1:10 molar ratio) and incubated for at least 1 h under gentle shaking at 25 °C. The remaining RhB was eliminated by filtering the enzyme solution in a tangential ultrafiltration unit (10 kDa) with 25 mM sodium phosphate-buffered solution at pH 7 until no fluorescence was detected in the filtered solution.

Enzyme Immobilization on Activated Carrier and Polycation Coating. For the enzyme immobilization, agarose microbeads were activated with epoxy groups and iminodiacetic acid (IDA), as described elsewhere.[32] Subsequently, the microbeads activated with IDA groups were incubated with a CoCl$_2$ solution of 30 mg mL^{-1} to synthesize the heterofunctional carrier containing both reactive Co^{2+} chelates and epoxy groups (AG-Co^{2+}/E). Then, 0.1 mg mL^{-1} pure and rhodamine B-labeled enzyme solution in 25 mM sodium phosphate buffer at pH 7 was incubated with AG-Co^{2+}/E in a ratio of 1:10 (w/v) for 1 h at 4 °C, and then washed with 25 mM sodium phosphate buffer at pH 7. Then, a solution of either PEI or PAH of 10 mg mL^{-1} at pH 8 was incubated with the immobilized enzyme in a ratio of 1:10 (w/v) for 1 h at room temperature. In the case of PDADMAC, the immobilized enzyme was first incubated overnight at 4 °C with 0.5 M aspartic acid in a ratio of 1:10 (w/v) to block the remaining epoxy groups and activate the surface with negative charges. Subsequently, the blocked resin was incubated with a PDADMAC solution of 10 mg mL^{-1} at pH 8 for 1 h at room temperature. Finally, the microbeads coated with the cationic polymers were washed 3 times with 10 mM Tris−HCl buffer at pH 7.

SDS-PAGE Analysis. Bs-ADH immobilized on AG-Co^{2+}/E carriers (resin) was analyzed by SDS-PAGE (Figure S1). Briefly, a 1:3 (w/v) suspension of resin with Laemmli buffer was boiled in a water bath for 5 min. Then, the samples were centrifuged at 9391g and the supernatant was withdrawn and loaded in the SDS-PAGE gel and run as described in standard molecular biology protocols.[62] The gel was stained with Coomassie and imaged with a Gel Doc EZ Gel documentation system (BIORAD).

X-ray Photoelectron Spectroscopy Measurements (XPS). XPS measurements were carried out using a suspension (1:10, w/v) of Bs-ADH immobilized on AG-Co^{2+}/E and coated with the corresponding polycation. This suspension was placed on top of silicon wafers and left to dry overnight at room temperature. XPS experiments were performed in a SPECS Sage HR 100 spectrometer with a nonmonochromatic X-ray source (magnesium Kα line of 1253.6 eV energy and 252 W), placed perpendicular to the analyzer axis and calibrated using the 3d$_{5/2}$ line of Ag with a full width at half maximum (FWHM) of 1.1 eV. The selected resolution for the spectra was 15 eV of pass energy and 0.15 eV/step. All measurements were made in an ultra-high vacuum (UHV) chamber at a pressure of around 8×10^{-8} mbar. An electron flood gun was used to neutralize charging. C 1s sp^3 from adventitious carbon was used for charge-correcting the spectra and fixed at 284.8 eV. The survey spectra were used for quantification (Table S1), and peak assignation was done according to JF Moulder[63] and NIST database.[64]

Cofactor Immobilization and Lixiviation Studies. Ionic immobilization of phosphorylated cofactors was achieved by incubating 10 volumes of a cofactor solution at the indicated concentration in 10 mM Tris−HCl at pH 7, with 1 volume of AG-Co^{2+}/E resin where enzymes had been previously immobilized subsequently coated with a polycation: PEI, PAH, or PDADMAC. The suspension was kept under orbital agitation at 25 rpm for 1 h at room temperature and finally filtered and washed three times with 10 mM Tris−HCl at pH 7. The concentration of the immobilized cofactors and their immobilization yield (% Ψ) was quantified by measuring the absorbance of the supernatants after adsorption and after 3 washing steps at the wavelength corresponding to each cofactor (340 nm for NAD(P)H, 450 nm for FAD, and 390 nm for PLP) in an Epoch 2 Microplate Spectrophotometer (BioTek instruments). In all cases, the cofactors lixiviation was followed by performing several washing steps after the immobilization while measuring the absorbance at each washing step.

Langmuir Isotherms and Binding Thermodynamics. Steady-state dissociation constant (K_D) and maximum adsorption capacity (q_{max}) of the different phosphorylated cofactors adsorbed on AG-Co^{2+}/E carriers coated with different cationic polymers were quantified from Langmuir adsorption isotherms (Figures S4 and S10) for NAD(P)H, FAD, FMN, and PLP toward each polymer. To obtain the adsorption isotherms, 1 mL of cofactor (0.05−4 mM) was incubated with 100 mg of each immobilized biocatalyst coated with the different polymers for 1 h at 30 °C. The supernatant after that incubation was collected and quantified by UV−vis (340 nm for NAD(P)H, 450 nm for FAD, and 390 nm for PLP) using an Epoch 2 Microplate reader. Finally, the absorbance values of the offered solution and the supernatant after the incubation were used to calculate the concentration of the bound cofactor at equilibrium (q_e) in μmoles g^{-1} and the

concentration of the nonbound cofactor in the supernatant at equilibrium (C_e) in mM. Where q_e and C_e were calculated using the following formulas

$$C_e = [\text{cofactor}]_{\text{sol}}, \quad q_e$$

$$= ([\text{cofactor}]_{\text{off}} - [\text{cofactor}]_{\text{sol}}) x \left(\frac{\text{bulk volume}}{\text{carrier mass}} \right)$$

where sol is the concentration of the cofactors in solution in the steady state and off is the offered cofactor concentration at time zero.

Confocal Laser Scanning Microscopy. Spatial organization of co-immobilized enzymes labeled with RhB and autofluorescent cofactors was followed using confocal laser scanning microscopy with a ZEISS LSM 880 (Carl, Zeiss, Germany) and excitation lasers of $\lambda_{\text{ex}} = 488$ nm for FAD, $\lambda_{\text{ex}} = 561$ nm for RhB-labeled enzymes, and $\lambda_{\text{ex}} = 405$ nm for NADH and PLP. Image processing of confocal images was performed using FIJI,[65] while scatterplots shown in Figure S3 were derived using the Ezcolocalization[66] plugin in the same software. Colocalization percentages were calculated by counting those pixels that were greater than the chosen threshold (10 000 a.u.) for both channels, represented by a yellow area in scatterplots of Figure S3.

Fluorescence Recovery after Photobleaching (FRAP) Measurements. Measurements were performed with a ZEISS LSM 880 (Carl, Zeiss, Germany) equipped with an argon laser (488 nm laser was used for the excitation of the FAD autofluorescent cofactor) and a 40× (oil, 1.2 NA) immersion objective. AG-Co^{2+}/E microbeads were coated with the different polycations PEI, PAH, and PDADMAC, and then 150 μM FAD in 10 mM Tris−HCl at pH 7 was incubated as previously described. FRAP measurements and analysis to extract FAD diffusion were performed according to Axelrod et al.,[67] Soumpasis et al.,[68] and Lopez et al.[69] The diameter of the bleached spot (round shaped) was 93 μm, and it was photobleached with an argon laser (100% laser intensity) for 5 s, while at the same time, a nonbleached spot of the same size of another microbead of similar size was considered as a reference for further corrections of focus drift, bleaching, and/or loss of intensity during image acquisition. Such corrections included the normalization of the obtained raw fluorescence intensity data after photobleaching with the corresponding fluorescence intensity data obtained from the nonbleached spot by applying the equation described by Soumpasis et al.[68] Detailed analysis of the normalized fluorescence recovery curves, as well as details related to the applied fitting method to derive affinity parameters toward the different polycations are described in the Results section.

Real-Time Activity Assays through *In Operando* Time-Lapse Fluorescence Microscopy. Different redox reactions were performed using a Cytation5 Cell Imaging Reader (BioTek Instruments) on a clear bottom, black 96-well microplate. The sample was observed with a Plan Fluorite 4X phase objective with a numerical aperture of 0.13 and coupled to an apotome grid WD with a working distance of 17 mm. DAPI ($\lambda_{\text{ex}} = 365$ nm/$\lambda_{\text{em}} = 447/90$ nm) and RFP ($\lambda_{\text{ex}} = 531$ nm/$\lambda_{\text{em}} = 593/40$ nm) imaging LED/filters pairs were used for fluorescence imaging of NAD(P)H/PLP and RhD-labeled enzymes, respectively. In parallel, the brightfield channel was also recorded to detect any change in the position of the microbeads during the experiment, avoiding any artifact that may interfere with the subsequent image analysis.

For the time-lapse experiments, a suspension of 1:400 (w/v) of AG-Co^{2+}/E coated with different polymers in 10 mM Tris−HCl at pH 7 was prepared. This suspension was placed into the well under microscopic analysis. Then, 0.1 mM NAD(P)H or PLP solution in 10 mM Tris−HCl at pH 7 was added into the well, and the cofactor immobilization was recorded every 5 s through time-lapse fluorescence microscopy imaging in the DAPI channel for 5 min. Finally, reactions were triggered either with 65 mM acetone in 10 mM Tris−HCl at pH 7, 150 μM Rf, FMN, or FAD in 10 mM Tris−HCl at pH 7, 10 mM dihydroxyacetone in 10 mM Tris−HCl, and with 2 mM rac-phenylethylamine in 10 mM Tris−HCl at pH 7 to measure the activity of Bs-ADH, Lp-NOX, Bs-KRED, and Pf-TA, respectively. The fluorescence decay of the reactions was monitored every 8 s through NAD(P)H or PLP time-lapse imaging in the DAPI channel until no fluorescence of NAD(P)H or PLP was detected. As a negative control, we incubated the same suspension containing both co-immobilized enzyme and cofactors under the same conditions but without exogenously adding the corresponding substrate (i.e., acetone) so that no reaction would occur. We confirmed that the single-particle fluorescence remains stable during the analysis time, demonstrating that the immobilized cofactor does not suffer any photobleaching. Further image processing and analysis were performed with a FIJI plugin recently developed in our group.[23] Through these analyses, we obtained ROIs of at least 10 microbeads and quantified the relative fluorescence units (RFUs) of each ROI at each time point of the acquired set of images. Likewise, we recorded the fluorescence corresponding to the RhB-labeled enzymes before starting the time-lapse experiment. Fluorescence intensity values were then divided by the volume of the corresponding ROI to calculate the integrated volumetric fluorescence of each cofactor at each time point and of each enzyme at time 0. Fluorescence standard curves were obtained for each fluorescently labeled enzyme and each cofactor using known concentrations of both and measured under the same conditions as those of the time-lapse experiments. These calibration curves enabled us to quantify the enzyme and cofactor concentrations (μM) inside the particles before the reaction started and during all reaction time points to construct the single-particle reaction courses. Time courses were then fitted using originLab[70] to derive enzyme apparent kinetic parameters toward the confined phosphorylated cofactor from single-particle analysis. The initial rate (V_o) of each reaction time course was calculated from the slope obtained from the linear fitting of the experimental data points at the beginning of the reaction progress, where the reaction course is still linear. The apparent Michaelis−Menten parameters were determined by fitting the time courses to the closed-form solution of the Michaelis−Menten equation,[46] expressed by the Lambert W-function.[47] For intraparticle analysis, our group has modified the previously mentioned developed image analytics plugin to derive information contained in one pixel. To obtain the average fluorescence intensity of all pixels located at the same distance from the center of one microbead, we utilized the plugin, and the routine is explained in detail elsewhere.[23]

Statistical Analysis of Single-Particle Studies. Statistical analysis of kinetic parameters of Bs-ADH co-immobilized with NADH on AG-Co^{2+}/E-PAH carriers was performed on data ($n > 10$) obtained from single-particle kinetics studies. The evaluated parameters were V_o, k_{cat}, K_M, k_{cat}/K_M, particle radius, enzyme concentration, and cofactor

concentration. The statistical data were obtained to establish possible correlations between the V_o, enzyme concentration, and k_{cat}/K_M versus the particle radius, k_{cat}, K_M, and k_{cat}/K_M versus the enzyme concentration, and k_{cat}/K_M versus the cofactor concentration. For this purpose, we calculated Pearson's correlation coefficient (r) and the P-value, which were determined by linear regression in OriginLab and by a one-way ANOVA single factor, respectively. Pearson's correlation coefficient and the P-value are indicated in each figure legend. A P-value of <0.05 was considered significant. For every correlation determined with the ANOVA single factor in Figures 6 and S11, the degree of freedom was 32, and in Figure S14A, the degree of freedom was 12, while F-values of every correlated pair are displayed in Table S2.

Principal component analysis (PCA) of single-particle reaction time courses. PCA[71] of a set of obtained time courses of NADH oxidation on AG-Co^{2+}/E-PAH carriers having Bs-ADH immobilized with different spatial organizations in the presence of 50 and 200 mM imidazole (Figure 8C) was performed to identify the number of distinct species in the sample. For PCA analysis, we have used originLab,[70] where the obtained time courses were assembled column-wise into matrix A, and the eigenvectors and the eigenvalues of the matrix AA^T were calculated (A^T is the matrix transpose of A). Two of the calculated eigenvalues had considerably larger values than the remaining eigenvalues for both time courses with Bs-ADH immobilized in the presence of 50 and 200 mM imidazole. This means that two components (species) are sufficient to describe the experimental curves.

■ ASSOCIATED CONTENT

Ⓢ Supporting Information

The Supporting Information is available free of charge at https://pubs.acs.org/doi/10.1021/acscatal.1c03760.

Figures S1–S15, and Tables S1 and S2 contain XPS analysis, colocalization analysis, Langmuir isotherms, additional single-particle time courses, cofactor lixiviation, and stability experiments among others (PDF)

■ AUTHOR INFORMATION

Corresponding Author

Fernando López-Gallego − *Center for Cooperative Research in Biomaterials (CIC biomaGUNE)—Basque Research and Technology Alliance (BRTA), 20014 Donostia-San Sebastián, Spain; IKERBASQUE, Basque Foundation for Science, 48013 Bilbao, Spain;* ● orcid.org/0000-0003-0031-1880; Email: flopez@cicbiomagune.es

Authors

Eleftheria Diamanti − *Center for Cooperative Research in Biomaterials (CIC biomaGUNE)—Basque Research and Technology Alliance (BRTA), 20014 Donostia-San Sebastián, Spain*

Javier Santiago-Arcos − *Center for Cooperative Research in Biomaterials (CIC biomaGUNE)—Basque Research and Technology Alliance (BRTA), 20014 Donostia-San Sebastián, Spain*

Daniel Grajales-Hernández − *Center for Cooperative Research in Biomaterials (CIC biomaGUNE)—Basque Research and Technology Alliance (BRTA), 20014 Donostia-San Sebastián, Spain*

Nicolette Czarnievicz − *Center for Cooperative Research in Biomaterials (CIC biomaGUNE)—Basque Research and Technology Alliance (BRTA), 20014 Donostia-San Sebastián, Spain*

Natalia Comino − *Center for Cooperative Research in Biomaterials (CIC biomaGUNE)—Basque Research and Technology Alliance (BRTA), 20014 Donostia-San Sebastián, Spain*

Irantzu Llarena − *Center for Cooperative Research in Biomaterials (CIC biomaGUNE)—Basque Research and Technology Alliance (BRTA), 20014 Donostia-San Sebastián, Spain*

Desiré Di Silvio − *Center for Cooperative Research in Biomaterials (CIC biomaGUNE)—Basque Research and Technology Alliance (BRTA), 20014 Donostia-San Sebastián, Spain*

Aitziber L. Cortajarena − *Center for Cooperative Research in Biomaterials (CIC biomaGUNE)—Basque Research and Technology Alliance (BRTA), 20014 Donostia-San Sebastián, Spain; IKERBASQUE, Basque Foundation for Science, 48013 Bilbao, Spain;* ● orcid.org/0000-0002-5331-114X

Complete contact information is available at:
https://pubs.acs.org/10.1021/acscatal.1c03760

Author Contributions

F.L.-G. conceptualized and supervised the study. E.D., J.S.-A., D.G.-H., N.C., N.C., and D.D.S. conducted the investigation. E.D. curated the data and did the formal analysis. E.D. and F.L.-G. designed the methodology. E.D. and F.L.-G. wrote the manuscript. All authors discussed the results and reviewed the manuscript.

Notes

The authors declare no competing financial interest.

■ ACKNOWLEDGMENTS

■ ABBREVIATIONS

Bs-ADH, NADH-dependent alcohol dehydrogenase from *B. stearothermophilus*; Lp-NOX, flavin-dependent NADH oxidase from *L. pentosus*; Bs-KRED, NADPH-dependent ketoreductase from *B. subtilis*; Pf-TA, pyridoxal-dependent transaminase from *P. fluorescence*; NAD(P)H, nicotinamide adenine dinucleotide phosphate; PLP, pyridoxal phosphate; FAD, flavin adenine dinucleotide; AG-Co^{2+}/E, agarose beads activated with cobalt chelates and epoxy groups; PEI, polyethyleneimine; PAH, polyallylamine; PDADMAC, polydiallyldimethylammonium chloride

■ REFERENCES

(1) Di Cosimo, R.; Mc Auliffe, J.; Poulose, A. J.; Bohlmann, G. Industrial Use of Immobilized Enzymes. *Chem. Soc. Rev.* **2013**, *42*, 6437−6474.

(2) Guisan, J. M.; Bolivar, J. M.; López-gallego, F. *Immobilization of Enzymes and Cells*; Guisan, J. M.; Bolivar, J. M.; López-Gallego, F.; Rocha-Martín, J., Eds.; Methods in Molecular Biology; Springer US: New York, NY, 2020; Vol. *2100*.

(3) Bommarius, A. S.; Paye, M. F. Stabilizing Biocatalysts. *Chem. Soc. Rev.* **2013**, *42*, 6534−6565.

(4) Brena, B.; González-Pombo, P.; Batista-Viera, F. Immobilization of Enzymes: A Literature Survey. In *Immobilization of Enzymes and Cells*, 3rd ed.; Guisan, J. M., Ed.; Methods in Molecular Biology; Humana Press: Totowa, NJ, 2013; Vol. *1051*, pp 15−31.

(5) Garcia-Galan, C.; Berenguer-Murcia, Á.; Fernandez-Lafuente, R.; Rodrigues, R. C. Potential of Different Enzyme Immobilization Strategies to Improve Enzyme Performance. *Adv. Synth. Catal.* **2011**, *353*, 2885−2904.

(6) Sheldon, R. A.; Pereira, P. C. Biocatalysis Engineering: The Big Picture. *Chem. Soc. Rev.* **2017**, *46*, 2678−2691.

(7) Kalz, K. F.; Kraehnert, R.; Dvoyashkin, M.; Dittmeyer, R.; Gläser, R.; Krewer, U.; Reuter, K.; Grunwaldt, J.-D. Future Challenges in Heterogeneous Catalysis: Understanding Catalysts under Dynamic Reaction Conditions. *ChemCatChem* **2017**, *9*, 17−29.

(8) Bolivar, J. M.; Nidetzky, B. On the Relationship between Structure and Catalytic Effectiveness in Solid Surface-Immobilized Enzymes: Advances in Methodology and the Quest for a Single-Molecule Perspective. *Biochim. Biophys. Acta, Proteins Proteomics* **2020**, *1868*, No. 140333.

(9) Bayne, L.; Ulijn, R. V.; Halling, P. J. Effect of Pore Size on the Performance of Immobilised Enzymes. *Chem. Soc. Rev.* **2013**, *42*, 9000−9010.

(10) Kovarik, M. L.; Allbritton, N. L. Measuring Enzyme Activity in Single Cells. *Trends Biotechnol.* **2011**, *29*, 222−230.

(11) Liu, L.; Chen, D.; Wang, J.; Chen, J. Advances of Single-Cell Protein Analysis. *Cells* **2020**, *9*, No. 1271.

(12) Zotter, A.; Bäuerle, F.; Dey, D.; Kiss, V.; Schreiber, G. Quantifying Enzyme Activity in Living Cells. *J. Biol. Chem.* **2017**, *292*, 15838−15848.

(13) Bolivar, J. M.; Eisl, I.; Nidetzky, B. Advanced Characterization of Immobilized Enzymes as Heterogeneous Biocatalysts. *Catal. Today* **2016**, *259*, 66−80.

(14) Benítez-Mateos, A. I.; Nidetzky, B.; Bolivar, J. M.; López-Gallego, F. Single-Particle Studies to Advance the Characterization of Heterogeneous Biocatalysts. *ChemCatChem* **2018**, *10*, 654−665.

(15) Joo, C.; Balci, H.; Ishitsuka, Y.; Buranachai, C.; Ha, T. Advances in Single-Molecule Fluorescence Methods for Molecular Biology. *Annu. Rev. Biochem.* **2008**, *77*, 51−76.

(16) Kienle, D. F.; Falatach, R. M.; Kaar, J. L.; Schwartz, D. K. Correlating Structural and Functional Heterogeneity of Immobilized Enzymes. *ACS Nano* **2018**, *12*, 8091−8103.

(17) Weltz, J. S.; Kienle, D. F.; Schwartz, D. K.; Kaar, J. L. Reduced Enzyme Dynamics upon Multipoint Covalent Immobilization Leads to Stability-Activity Trade-Off. *J. Am. Chem. Soc.* **2020**, *142*, 3463−3471.

(18) Chaparro Sosa, A. F.; Bednar, R. M.; Mehl, R. A.; Schwartz, D. K.; Kaar, J. L. Faster Surface Ligation Reactions Improve Immobilized Enzyme Structure and Activity. *J. Am. Chem. Soc.* **2021**, *143*, 7154−7163.

(19) Cantone, S.; Ferrario, V.; Corici, L.; Ebert, C.; Fattor, D.; Spizzo, P.; Gardossi, L. Efficient Immobilisation of Industrial Biocatalysts: Criteria and Constraints for the Selection of Organic Polymeric Carriers and Immobilisation Methods. *Chem. Soc. Rev.* **2013**, *42*, 6262−6276.

(20) Schmid-Dannert, C.; López-Gallego, F. Advances and Opportunities for the Design of Self-Sufficient and Spatially Organized Cell-Free Biocatalytic Systems. *Curr. Opin. Chem. Biol.* **2019**, *49*, 97−104.

(21) Velasco-Lozano, S.; Benítez-Mateos, A. I.; López-Gallego, F. Co-Immobilized Phosphorylated Cofactors and Enzymes as Self-Sufficient Heterogeneous Biocatalysts for Chemical Processes. *Angew. Chem., Int. Ed.* **2017**, *56*, 771−775.

(22) Benítez-Mateos, A. I.; San Sebastian, E.; Ríos-Lombardía, N.; Morís, F.; González-Sabín, J.; López-Gallego, F. Asymmetric Reduction of Prochiral Ketones by Using Self-Sufficient Heterogeneous Biocatalysts Based on NADPH-Dependent Ketoreductases. *Chem. - Eur. J.* **2017**, *23*, 16843−16852.

(23) Muñoz-Morales, E.; Velasco-Lozano, S.; Benítez-Mateos, A. I.; Marín, M. J.; Ramos-Cabrer, P.; López-Gallego, F. Deciphering the Effect of Microbead Size Distribution on the Kinetics of Heterogeneous Biocatalysts through Single-Particle Analysis Based on Fluorescence Microscopy. *Catalysts* **2019**, *9*, No. 896.

(24) Benítez-Mateos, A. I.; Contente, M. L.; Velasco-Lozano, S.; Paradisi, F.; López-Gallego, F. Self-Sufficient Flow-Biocatalysis by Coimmobilization of Pyridoxal 5′-Phosphate and ω-Transaminases onto Porous Carriers. *ACS Sustainable Chem. Eng.* **2018**, *6*, 13151−13159.

(25) Contente, M. L.; Paradisi, F. Self-Sustaining Closed-Loop Multienzyme-Mediated Conversion of Amines into Alcohols in Continuous Reactions. *Nat. Catal.* **2018**, *1*, 452−459.

(26) Mateo, C.; Grazu, V.; Palomo, J. M.; Lopez-Gallego, F.; Fernandez-Lafuente, R.; Guisan, J. M. Immobilization of Enzymes on Heterofunctional Epoxy Supports. *Nat. Protoc.* **2007**, *2*, 1022−1033.

(27) Ceccarelli, C.; Liang, Z.-X.; Strickler, M.; Prehna, G.; Goldstein, B. M.; Klinman, J. P.; Bahnson, B. J. Crystal Structure and Amide H/D Exchange of Binary Complexes of Alcohol Dehydrogenase from *Bacillus stearothermophilus*: Insight into Thermostability and Cofactor Binding. *Biochemistry* **2004**, *43*, 5266−5277.

(28) Nowak, C.; Beer, B.; Pick, A.; Roth, T.; Lommes, P.; Sieber, V. A Water-Forming NADH Oxidase from *Lactobacillus pentosus* Suitable for the Regeneration of Synthetic Biomimetic Cofactors. *Front. Microbiol.* **2015**, *6*, No. 957.

(29) Ni, Y.; Li, C. X.; Ma, H. M.; Zhang, J.; Xu, J. H. Biocatalytic Properties of a Recombinant Aldo-Keto Reductase with Broad Substrate Spectrum and Excellent Stereoselectivity. *Appl. Microbiol. Biotechnol.* **2011**, *89*, 1111−1118.

(30) Roura Padrosa, D.; Alaux, R.; Smith, P.; Dreveny, I.; López-Gallego, F.; Paradisi, F. Enhancing PLP-Binding Capacity of Class-III ω-Transaminase by Single Residue Substitution. *Front. Bioeng. Biotechnol.* **2019**, *7*, No. 282.

(31) Santiago-Arcos, J.; Velasco-Lozano, S.; Diamanti, E.; Cortajarena, A. L.; López-Gallego, F. Immobilization Screening and Characterization of an Alcohol Dehydrogenase and Its Application to the Multi-Enzymatic Selective Oxidation of 1,-Omega-Diols. *Front. Catal.* **2021**, *1*, No. 715075.

(32) Benítez-Mateos, A. I.; Contente, M. L.; Velasco-Lozano, S.; Paradisi, F.; López-Gallego, F. Self-Sufficient Flow-Biocatalysis by Coimmobilization of Pyridoxal 5′-Phosphate and ω-Transaminases onto Porous Carriers. *ACS Sustainable Chem. Eng.* **2018**, *6*, 13151−13159.

(33) Sparks, D. L. Sorption Phenomena on Soils. In *Environmental Soil Chemistry*; Elsevier, 2003; pp 133−186.

(34) Diamanti, E.; Cuellar, L.; Gregurec, D.; Moya, S. E.; Donath, E. Role of Hydrogen Bonding and Polyanion Composition in the Formation of Lipid Bilayers on Top of Polyelectrolyte Multilayers. *Langmuir* **2015**, *31*, 8623−8632.

(35) Diamanti, E.; Andreozzi, P.; Anguiano, R.; Yate, L.; Gregurec, D.; Politakos, N.; Ziolo, R. F.; Donath, E.; Moya, S. E. The Effect of Top-Layer Chemistry on the Formation of Supported Lipid Bilayers on Polyelectrolyte Multilayers: Primary versus Quaternary Amines. *Phys. Chem. Chem. Phys.* **2016**, *18*, 32396−32405.

(36) Demadis, K. D.; Paspalaki, M.; Theodorou, J. Controlled Release of Bis(Phosphonate) Pharmaceuticals from Cationic Biodegradable Polymeric Matrices. *Ind. Eng. Chem. Res.* **2011**, *50*, 5873−5876.

(37) Dickhaus, B. N.; Priefer, R. Determination of Polyelectrolyte PKa Values Using Surface-to-Air Tension Measurements. *Colloids Surf., A* **2016**, *488*, 15−19.

(38) Sprague, B. L.; Pego, R. L.; Stavreva, D. A.; McNally, J. G. Analysis of Binding Reactions by Fluorescence Recovery after Photobleaching. *Biophys. J.* **2004**, *86*, 3473−3495.

(39) Mueller, F.; Wach, P.; McNally, J. G. Evidence for a Common Mode of Transcription Factor Interaction with Chromatin as Revealed by Improved Quantitative Fluorescence Recovery after Photobleaching. *Biophys. J.* **2008**, *94*, 3323−3339.

(40) Sprague, B. L.; McNally, J. G. FRAP Analysis of Binding: Proper and Fitting. *Trends Cell Biol.* **2005**, *15*, 84−91.

(41) McNally, J. G. Quantitative FRAP in Analysis of Molecular Binding Dynamics In Vivo. *Methods Cell Biol.* **2008**, *85*, 329−351.

(42) Braga, J.; McNally, J. G.; Carmo-Fonseca, M. A Reaction-Diffusion Model to Study RNA Motion by Quantitative Fluorescence Recovery after Photobleaching. *Biophys. J.* **2007**, *92*, 2694−2703.

(43) Rover, L.; Fernandes, J. C. B.; Neto, G. D. O.; Kubota, L. T.; Katekawa, E.; Serrano, S. H. P. Study of NADH Stability Using Ultraviolet-Visible Spectrophotometric Analysis and Factorial Design. *Anal. Biochem.* **1998**, *260*, 50−55.

(44) Yamamoto, K.; Morikawa, K.; Imanaka, H.; Imamura, K.; Kitamori, T. Picoliter Enzyme Reactor on a Nanofluidic Device Exceeding the Bulk Reaction Rate. *Analyst* **2020**, *145*, 5801−5807.

(45) Kienle, D. F.; Chaparro Sosa, A. F.; Kaar, J. L.; Schwartz, D. K. Polyelectrolyte Multilayers Enhance the Dry Storage and PH Stability of Physically Entrapped Enzymes. *ACS Appl. Mater. Interfaces* **2020**, *12*, 22640−22649.

(46) Beal, S. L. On the Solution to the Michaelis-Menten Equation. *J. Pharmacokinet. Biopharm.* **1982**, *10*, 109−119.

(47) Schnell, S.; Mendoza, C.; Mendoza, S. S. C. Closed Form Solution for Time-Dependent Enzyme Kinetics. *J. Theor. Biol.* **1997**, *187*, 207−212.

(48) Goličnik, M. On the Lambert W Function and Its Utility in Biochemical Kinetics. *Biochem. Eng. J.* **2012**, *63*, 116−123.

(49) Benítez-Mateos, A. I.; Huber, C.; Nidetzky, B.; Bolivar, J. M.; López-Gallego, F. Design of the Enzyme−Carrier Interface to Overcome the O 2 and NADH Mass Transfer Limitations of an Immobilized Flavin Oxidase. *ACS Appl. Mater. Interfaces* **2020**, *12*, 56027−56038.

(50) Chen, B.; Miller, E. M.; Miller, L.; Maikner, J. J.; Gross, R. A. Effects of Macroporous Resin Size on Candida Antarctica Lipase B Adsorption, Fraction of Active Molecules, and Catalytic Activity for Polyester Synthesis. *Langmuir* **2007**, *23*, 1381−1387.

(51) Valencia, P.; Wilson, L.; Aguirre, C.; Illanes, A. Evaluation of the Incidence of Diffusional Restrictions on the Enzymatic Reactions of Hydrolysis of Penicillin G and Synthesis of Cephalexin. *Enzyme Microb. Technol.* **2010**, *47*, 268−276.

(52) Shuler, M. L.; Tsuchiya, H. M.; Aris, R. Diffusive and Electrostatic Effects with Insolubilized Enzymes Subject to Substrate Inhibition. *J. Theor. Biol.* **1973**, *41*, 347−356.

(53) Schnell, S.; Turner, T. E. Reaction Kinetics in Intracellular Environments with Macromolecular Crowding: Simulations and Rate Laws. *Prog. Biophys. Mol. Biol.* **2004**, *85*, 235−260.

(54) Minton, A. P.; Wilf, J. Effect of Macromolecular Crowding upon the Structure and Function of an Enzyme: Glyceraldehyde-3-Phosphate Dehydrogenase. *Biochemistry* **1981**, *20*, 4821−4826.

(55) Ma, B.; Nussinov, R. Structured Crowding and Its Effects on Enzyme Catalysis. In *Dynamics in Enzyme Catalysis*; Springer, 2013; Vol. *310*, pp 123−137.

(56) Schroeder, M. M.; Wang, Q.; Badieyan, S.; Chen, Z.; Marsh, E. N. G. Effect of Surface Crowding and Surface Hydrophilicity on the Activity, Stability and Molecular Orientation of a Covalently Tethered Enzyme. *Langmuir* **2017**, *33*, 7152−7159.

(57) Zaak, H.; Siar, E. H.; Kornecki, J. F.; Fernandez-Lopez, L.; Pedrero, S. G.; Virgen-Ortíz, J. J.; Fernandez-Lafuente, R. Effect of Immobilization Rate and Enzyme Crowding on Enzyme Stability under Different Conditions. The Case of Lipase from Thermomyces

Lanuginosus Immobilized on Octyl Agarose Beads. *Process Biochem.* **2017**, *56*, 117−123.

(58) Balevicius, Z.; Ignatjeva, D.; Niaura, G.; Ignatjev, I.; Vaicikauskas, V.; Babonas, G. J.; Valincius, G. Crowding Enhances Lipase Turnover Rate on Surface-Immobilized Substrates. *Colloids Surf., B* **2015**, *131*, 115−121.

(59) Bolivar, J. M.; Hidalgo, A.; Sánchez-Ruiloba, L.; Berenguer, J.; Guisán, J. M.; López-Gallego, F. Modulation of the Distribution of Small Proteins within Porous Matrixes by Smart-Control of the Immobilization Rate. *J. Biotechnol.* **2011**, *155*, 412−420.

(60) Rocha-Martín, J.; Rivas, B. D. L.; Muñoz, R.; Guisán, J. M.; López-Gallego, F. Rational Co-Immobilization of Bi-Enzyme Cascades on Porous Supports and Their Applications in Bio-Redox Reactions with Insitu Recycling of Soluble Cofactors. *ChemCatChem* **2012**, *4*, 1279−1288.

(61) Schmid-Dannert, C.; López-Gallego, F. Advances and Opportunities for the Design of Self-Sufficient and Spatially Organized Cell-Free Biocatalytic Systems. *Curr. Opin. Chem. Biol.* **2019**, *49*, 97−104.

(62) Sambrook, J.; Fritsch, E. F.; Maniatis, T. *Molecular Cloning: A Laboratory Manual*; Cold Spring Harbor Laboratory Press: Cold Spring Harbor, NY, USA, 1989.

(63) Moulder, J. F.; Chastain, J. *Handbook of X-Ray Photoelectron Spectroscopy: A Reference Book of Standard Spectra for Identification and Interpretation of XPS Data*; Physical Electronics Division; Perkin-Elmer Corp: Eden Prairie, Minn, 1992.

(64) Rumble, J. R.; Bickham, D. M.; Powell, C. J. The NIST X-Ray Photoelectron Spectroscopy Database. *Surf. Interface Anal.* **1992**, *19*, 241−246.

(65) Bolte, S.; Cordelieres, F. P. A Guided Tour into Subcellular Colocalization Analysis in Light Microscopy. *J. Microsc.* **2006**, *224*, 213−232.

(66) Stauffer, W.; Sheng, H.; Lim, H. N. EzColocalization: An ImageJ Plugin for Visualizing and Measuring Colocalization in Cells and Organisms. *Sci. Rep.* **2018**, *8*, No. 15764.

(67) Axelrod, D.; Koppel, D. E.; Schlessinger, J.; Elson, E.; Webb, W. W. Mobility Measurement by Analysis of Fluorescence Photo-bleaching Recovery Kinetics. *Biophys. J.* **1976**, *16*, 1055−1069.

(68) Soumpasis, D. M. Theoretical Analysis of Fluorescence Photobleaching Recovery Experiments. *Biophys. J.* **1983**, *41*, 95−97.

(69) Lopez, A.; Dupou, L.; Altibelli, A.; Trotard, J.; Tocanne, J. F. Fluorescence Recovery after Photobleaching (FRAP) Experiments under Conditions of Uniform Disk Illumination. Critical Comparison of Analytical Solutions, and a New Mathematical Method for Calculation of Diffusion Coefficient D. *Biophys. J.* **1988**, *53*, 963−970.

(70) *Origin*, v7.0; OriginLab Corporation: Northampton, MA, 2021.

(71) Shlens, J. A Tutorial on Principal Component Analysis. 2014, arXiv:1404.1100. arXiv.org e-Print archive. http://arxiv.org/abs/1404.1100.